Paper II

Eulerian-Eulerian Simulation of Heat Transfer Between a Gas-Solid Fluidized Bed and an Immersed Tube-Bank with Horizontal Tubes

Under review in *Chemical Engineering Science*

Eulerian-Eulerian Simulation of Heat Transfer Between a Gas-Solid Fluidized Bed and an Immersed Tube-Bank with Horizontal Tubes

Rahel Yusuf[1], Britt Halvorsen[1], and Morten Christian Melaaen[1,2]
[1]Telemark University College, Kjølnes Ring 56, 3918, Porsgrunn, Norway
[2]Telemark Technological R&D Centre (TEL-TEK), Kjølnes Ring 56, 3918, Porsgrunn, Norway

Abstract

A two dimensional Eulerian-Eulerian simulation of tube-to-bed heat transfer is carried out for a cold gas fluidized bed with immersed horizontal tubes. The horizontal tubes are modelled as obstacles with square cross section in the numerical model. Simulations are performed for two gas velocities exceeding the minimum fluidization velocity by 0.2 m/s and 0.6 m/s and two operating pressures of 0.1 MPa and 1.6 MPa. Local instantaneous and time averaged heat transfer coefficients are monitored at four different positions around the tube and compared against experimental data reported in literature. The role of constitutive equations for the solid phase thermal conductivity on heat transfer is investigated and a fundamental approach to model the solid phase thermal conductivity is implemented in the present work. Significant improvement in the agreement of the predicted and the measured local instantaneous heat transfer coefficient is observed in the present study when compared to the previous works which over predicted the local instantaneous heat transfer coefficient. At the atmospheric pressure, the local instantaneous heat transfer coefficient shows good agreement with the measured values both qualitatively and quantitatively. At the higher pressure, similar to the measurements, the predicted local instantaneous heat transfer coefficient shows an increase with increasing pressure. However, the agreement is more qualitative and quantitatively the maxima and minima of the local instantaneous heat transfer coefficient are under predicted. The local time averaged heat transfer coefficients are within 20 % of the measured values at the atmospheric pressure. In contrast, under prediction of the time averaged heat transfer coefficient is observed at the higher pressure.

1. Introduction

Gas-solid fluidized beds are an attractive choice in applications involving heat transfer by virtue of their high heat transfer rates. The vigorous particle motions inside the bed lead to heat convection across the bed thus making efficient heat transfer possible. Fluidized bed combustors (FBC) with immersed tubes are often used in power generation in order to utilize high heat transfer rates observed in gas-solid fluidized beds. The in-bed cooling tubes offer a large heat transfer area which in tandem with solids movements inside the bed leads to an efficient heat transfer setup.

In order to arrive at efficient designs of fluidized bed combustors with cooling tubes, the local heat transfer phenomena between the bed and tubes needs to be investigated. Many empirical correlations for heat transfer between a wall surface and a gas-solid fluidized bed have been presented in literature. A detailed review of some of the empirical equations for surface to bed heat transfer is presented in Yusuf et al. (2005).

The empirical correlations suffer from two drawbacks. Firstly, they are reliable only within the domain of operating conditions based on which they were arrived at. Secondly, they fail to provide a fundamental understanding of the underlying transport phenomena. The ever increasing computational power of present day computers makes computational fluid dynamic simulations a very attractive method to gain fundamental knowledge of complex processes which are otherwise difficult to quantize. The computational fluid dynamics (CFD) approach basically consists of numerically solving the Navier Stokes equation to obtain the flow field. By using the flow field hence obtained, thermal energy and/or species balance equation can be solved for the temperature and/or the species concentration field. The advantage with this approach is that it is based on first principles and requires fewer empirical inputs. The application of CFD to model gas-solid flows is however not so straightforward. While the gas phase can be modelled by the Navier Stokes equation, the description of solid phase poses

problems. The solid particles possess a discrete nature and in principle, the motion of each particle should be tracked by applying the laws of motion and accounting for gas-particle and particle-particle dynamics. However, dense gas-solid flows like bubbling beds also provide an opportunity to treat the solid phase as continuum like the gas phase. Hence, two approaches can be used to model gas-solid flows. The first approach is called the Eulerian-Lagrangian Approach. In the Eulerian-Lagrangian approach the CFD application is limited to the gas phase while each particle is tracked by solving the newtonian equation of motion in conjunction with a particle-particle and particle-wall collision model. The second approach is called the Eulerian-Eulerian approach which is also known as two fluid model (TFM). The Eulerian-Eulerian approach considers the solids as a continuum like the gas phase. Such an approach allows the solid phase to be described by the Navier Stokes equation akin to the gas phase.

Due to the presence of large number of particle in the fluidized bed, the computational cost associated with the Eulerian-Lagrangian approach can be overwhelming. In such a scenario, researchers have often turned to the Eulerian-Eulerian approach to investigate heat transfer in gas fluidized beds. In recent years, Kuipers et al. (1992), Patil et al. (2006) and Yusuf et al. (2008) have used Eulerian-Eulerian approach to study heat transfer from a heated wall to a laboratory scale two dimensional bed. For the numerical prediction of heat transfer from complex geometries like immersed tubes, only a couple of studies by Schmidt and Renz (2000, 2005) have been reported in literature. Schmidt and Renz (2000, 2005) studied local instantaneous heat transfer coefficient from immersed tube (s) in a two dimensional numerical setup for very short simulation runs of up to 1.4 seconds and reported higher heat transfer coefficients than the experimentally measured values. The difference between the predicted and measured values was much higher at the bottom of the tubes than at the top of the tube.

The application of Eulerian-Eulerian approach to heat transfer from immersed surfaces requires the constitutive equations for the thermal conductivities of the gas and solid phase in the bed core and in the vicinity of the immersed surface. The thermal conductivity of the solid phase in the bulk and in near wall (read as immersed surface henceforth) region can differ from the true thermal conductivity of the solid particles due to particle-particle contacts in the bulk and particle-wall contacts in the near wall region. The aforementioned studies on heat transfer from immersed tube (or tubes) to fluidized bed have obtained gas and solid phase thermal conductivities in the bulk and the near wall region from Zehner and Schluender (1970) model for gas-solid bulk thermal conductivity in the core of a packed bed. Zehner and Schluender model (1970) calculates the thermal conductivity of the gas-solid bulk as a function of bulk voidage and the true thermal conductivities of gas and solid particles on the basis of a unit cell in the bulk of the packed bed.

Legawiec and Ziolkowski (1994) have argued that heat is conducted more efficiently in the core of the bed than in the near wall region as the number of particle contacts per unit area in the bed core are higher than the number of particle-wall contacts in the near wall region for a given voidage. The aforementioned reasoning implies that solid phase thermal conductivity is higher in the bed core than in the near wall region. Since, Zehner and Schluender (1970) model is developed for the bed core, its extension to the near wall region could predict higher thermal conductivity for the solid phase in the near wall region eventually leading to high values of heat transfer coefficient between the immersed surface and the bed. The extension of Zehner and Schluender (1970) model to the near wall region seems to be the possible reason for the high values of heat transfer coefficients reported by Schmidt and Renz (2000, 2005).

A fundamental thermal conductivity model that is based on the background of heat transfer in the near wall bed region is thus needed to obtain realistic predictions of heat transfer between a wall surface and the fluidized bed.

From a design standpoint, time averaged values rather than the local instantaneous values of the predicted heat transfer coefficient are of more significance. Previous works of Schmidt and Renz (2005) have reported comparisons between the predicted and measured local time averaged heat transfer coefficients around the tube for a very short simulation averaging time of 1.4 seconds due to time intensive computations. Ideally, simulations should be run for longer time in order to obtain more realistic comparisons between the predicted values of the local time averaged heat transfer coefficient and the measurements as the measured time averaged heat transfer coefficient is generally obtained over a couple of minutes or even higher. Further, fluidized bed combustors operate at high pressures and the effect of pressure on the heat transfer coefficient is an area that has not been addressed in the studies on numerical simulation of heat transfer in fluidized beds with immersed tubes.

With only few studies involving numerical simulation of heat transfer between tube banks and fluidized bed being reported in literature and with aforementioned areas that require further attention, the present work aims to enhance the fundamental understanding of heat transfer phenomena in gas-fluidized beds with complex geometries like immersed tubes. In this work, an in-depth study into the influence of thermal conductivity of solid phase in the vicinity of a heated tube is conducted in order to address the underlying causes of the over prediction of tube to bed heat transfer coefficients in the previous works. Further, an investigation into the role of operating parameters like pressure and velocity on the local instantaneous and time averaged heat transfer coefficient is being carried out.

The numerical simulations in this study are based on the Eulerian-Eulerian approach. The system chosen for simulations is a cold pressurised laboratory scale fluidized bed used by

Olsson and Almstedt (1995) to measure local instantaneous bed to tube heat transfer coefficients. Numerical predictions are compared against the measurements of Olsson and Almstedt (1995).

2. Experimental

The experimental rig of Olsson and Amstedt (1995) was a 2.1m long plexiglass column with a rectangular cross-section of 0.2 m x 0.3 m. They used silica as bed material with a particle density of 2600 kg/m^3, a mean particle size of 700 microns and a form factor of 0.8. The mass of bed material used by them was 73 kg which corresponds to 0.86 m of bed height at minimum fluidization velocity with a minimum fluidization voidage of 0.46. They used three different tube-bank geometries named as I4, S4 and S4D. Only the geometry S4D is studied in the present work since local instantaneous heat transfer coefficients were reported by Olsson and Amstedt (1995) only for this geometry.

The tube-banks were made up of horizontal aluminium tubes with a diameter of 20 mm. In order to carry out heat transfer measurements, one of the aluminium tube was replaced by a tube with an inbuilt heater and a lengthwise central section made of copper. Heat flux sensors were mounted on the surface of the copper tube to measure heat flux. The copper tube was maintained at a temperature of 60 °C while the bed was operated at a temperature of 15 °C. The bed pressure was varied between 0.1 and 1.6 MPa. The bed was operated at two different gas velocities exceeding the minimum fluidization velocities by 0.2 m/s and 0.6 m/s. The local instantaneous heat transfer coefficient was measured around the heat transfer tube with 30 degree increments. The upward face was counted as the 0 degree position with angles counted counter clockwise. A schematic of the S4D tube configuration and the heat transfer tube are shown in Figure 1.

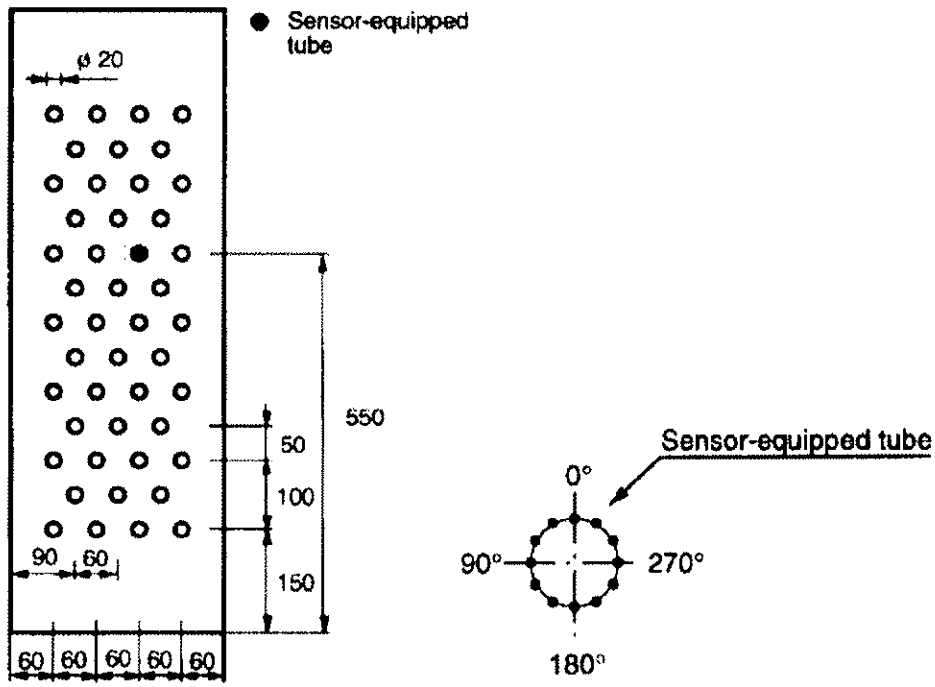

Figure 1 A schematic of S4D tube configuration of the experimental setup and measuring positions on the sensor equipped tube (Adapted from Olsson and Almstedt (1995)

3. Fluid dynamic model

The fluid dynamic model is based on the Eulerian-Eulerian approach that treats the gas and solid phases as interpenetrating continua. Separate conservation equations are formulated for both the phases. Since the solid phase is considered as a fluid, constitutive equations for the solid phase viscosity and pressure are required. In the present work, the constitutive equations are obtained from the kinetic theory of granular flows (KTGF). In KTGF, the solid viscosity and pressure are expressed in terms of a granular temperature which characterizes the random motion of particles (Gidaspow (1994)). An additional transport equation for the conservation of turbulent kinetic energy associated with random motion of particles is solved in order to obtain the distribution of granular temperature. Mathiesen et al. (1999, 2000) incorporated a KTGF model for multiple solid phases into the in-house code FLOTRACS-MP-3D. They also

included area and volume porosities in the governing equations in order to enable modelling of obstacles like immersed tubes. The volume/area porosities can take values between zero and one, where zero stands for a totally blocked area or volume while a value of one represents an open surface or volume. Only one solid phase is considered in the present work. For a single solid phase, the multiple solid phase model reduces to the same form as proposed by Gidaspow (1994) for one solid phase.

A frictional stress model is added to the fluid dynamic model in order to handle dense solid regions encountered in bubbling beds where sustained contacts between the particles give rise to tangential and normal frictional stresses. A thermal energy balance equation for each phase is added to the in-house code for heat transfer calculations. The detailed hydrodynamic model with KTGF for one solid phase is presented in the following subsections together with the frictional stress model and thermal energy balance equations which were added during the course of present work. All the conservation equations are presented in the cartesian tensor notations.

3.1 Continuity equations

Gas Phase:

$$\frac{\partial}{\partial t}\left(\beta_v \varepsilon_g \rho_g\right)+\frac{\partial}{\partial x_i}\left(\beta_i \varepsilon_g \rho_g U_{i,g}\right)=0 \tag{1}$$

Solid Phase:

$$\frac{\partial}{\partial t}\left(\beta_v \varepsilon_s \rho_s\right)+\frac{\partial}{\partial x_i}\left(\beta_i \varepsilon_s \rho_s U_{i,s}\right)=0 \tag{2}$$

where, t is time, ε is the volume fraction, ρ is the density, x_i is the coordinate in i direction, β_v is the volume porosity, β_i is the area porosity in i direction and U_i is the i direction velocity component. The subscripts g and s refer to the gas and solid phase respectively.

3.2 Momentum balance equations

The gas phase momentum balance in the j direction is written as

$$\frac{\partial}{\partial t}\left(\beta_v \varepsilon_g \rho_g U_{j,g}\right)+\frac{\partial}{\partial x_i}\left(\beta_i \varepsilon_g \rho_g U_{i,g} U_{j,g}\right)$$
$$=-\beta_v \varepsilon_g \frac{\partial P_g}{\partial x_j}+\frac{\partial\left(\beta_i \tau_{ij,g}\right)}{\partial x_j}+\beta_v \varepsilon_g \rho_g g_j+\beta_v \Phi_{gs}\left(U_{j,s}-U_{j,g}\right) \quad (3)$$

where, P is the fluid pressure, g_j is the j direction component of gravity and Φ_{gs} is the drag coefficient between the gas and solid phase. The stress tensor $\tau_{ij,g}$ in the gas phase is expressed as

$$\tau_{ij,g}=\varepsilon_g \mu_g\left[\left(\frac{\partial U_j}{\partial x_i}+\frac{\partial U_i}{\partial x_j}\right)-\frac{2}{3}\delta_{i,j}\frac{\partial U_k}{\partial x_k}\right] \quad (4)$$

where, μ_g is the laminar gas viscosity and $\delta_{i,j}$ is the Kroenecker delta.

The solid phase momentum balance in the j direction is written as

$$\frac{\partial}{\partial t}\left(\beta_v \varepsilon_s \rho_s U_{j,s}\right)+\frac{\partial}{\partial x_i}\left(\beta_i \varepsilon_s \rho_s U_{i,s} U_{j,s}\right)=$$
$$-\beta_v \varepsilon_s \frac{\partial P_g}{\partial x_j}+\frac{\partial\left(\beta_i \Pi_{ij,s}\right)}{\partial x_j}+\beta_v \varepsilon_s \rho_s g_j+\beta_v \Phi_{gs}\left(U_{j,g}-U_{j,s}\right) \quad (5)$$

Here, $\Pi_{ij,s}$ is the total stress tensor in the solid phase and expressed as

$$\Pi_{ij,s}=-P_s \delta_{ij}+\mu_s\left(\frac{\partial U_j}{\partial x_i}+\frac{\partial U_i}{\partial x_j}\right)_s+\left(\xi_s-\frac{2}{3}\mu_s\right)\delta_{ij}\left(\frac{\partial U_k}{\partial x_k}\right)_s \quad (6)$$

where, P_s is the solid pressure, μ_s is the shear viscosity of solids and ξ_s is the bulk viscosity of solids.

In the Eulerian-Eulerian model based on KTGF, the solid phase stress tensor is assumed to be a sum of a kinetic collision component and a frictional component. The kinetic collision component results from the random motion of particles which is characterized by a granular temperature while the frictional component of solid stresses comes into play when solids volume fraction is high leading to longer contacts between neighbouring particles. Such contacts give rise to frictional stresses which should be accounted for in dense systems like bubbling fluidized beds. The kinetic-collisional and frictional components are considered additive in accordance with the approach of Johnson and Jackson (1987) who argued that

each component should be evaluated as a separate entity. Following the additive nature of two components, the total solid phase pressure and viscosity can be expressed as

$$\begin{aligned} P_s &= P_s^{kc} + P_s^f \\ \mu_s &= \mu_s^{kc} + \mu_s^f \\ \xi_s &= \xi_s^{kc} + \xi_s^f \end{aligned} \tag{7}$$

where, superscript kc stands for kinetic-collisional contributions while f stands for the frictional contributions.

The kinetic-collisional components of pressure and viscosity are further expressed as

$$P_s^{kc} = \varepsilon_s \rho_s \left(1 + 2(1+e_s) g_0 \varepsilon_s\right) \theta_s \tag{8}$$

$$\xi_s^{kc} = \frac{4}{3} \varepsilon_s^2 \rho_s d_s g_0 (1+e_s) \sqrt{\frac{\theta_s}{\pi}} \tag{9}$$

$$\mu_s^{kc} = \frac{2\mu_{dil,s}}{(1+e_s) g_0} \left(1 + \frac{4}{5}(1+e_s) g_0 \varepsilon_s\right)^2 + \frac{4}{5} \varepsilon_s^2 \rho_s d_s g_0 (1+e_s) \sqrt{\frac{\theta_s}{\pi}} \tag{10}$$

$$\mu_{dil,s} = \frac{5}{96} \rho_s d_s \sqrt{\pi \theta_s} \tag{11}$$

Where, d_s is the particle diameter, e_s is the coefficient of restitution, g_0 is the radial distribution function, and θ_s is the granular temperature of the solid phase and l_s is the mean free path of solid particle. The expression for radial distribution function is taken from Ma and Ahmadi (1986) and has the following form

$$g_0 = \frac{1 + 2.5\varepsilon_s + 4.5904\varepsilon_s^2 + 4.515439\varepsilon_s^3}{\left[1 - \left(\frac{\varepsilon_s}{\varepsilon_s^{\max}}\right)^3\right]^{0.67802}} \tag{12}$$

where, $\varepsilon_s^{\max}$ is the maximum solid volume fraction and has a value equal to 0.64356.

While the constitutive equations for kinetic-collisional contributions are obtained from KTGF, models for frictional stresses are mostly based on the granular flows in soil mechanics. In the present work, the closure described by Srivastava and Sundaresan (2003) is used. Srivastava and Sundaresan (2003) modified the model of Schaeffer (1987) for a quasi static flow of a

solid assembly by accounting for fluctuations in strain rate. The complete closure can be expressed as

$$P_s^f = P_c(\varepsilon_s) \tag{13}$$

where, P_s^f is the frictional component of solids pressure, and $P_c(\varepsilon_s)$ is the critical state pressure given by Johnson and Jackson (1987) and expressed as

$$P_c(\varepsilon_s) = F\frac{(\varepsilon_s - \varepsilon_{s,\min})^a}{(\varepsilon_{s,\max} - \varepsilon_s)^b} \qquad \varepsilon_s > \varepsilon_{s,\min} \tag{14}$$

$$P_c(\varepsilon_s) = 0 \qquad \varepsilon_s < \varepsilon_{s,\min}$$

The frictional shear viscosity, μ_s^f for the solid phase is given by the following equation

$$\mu_s^f = \frac{P_c(\varepsilon_S)\sqrt{2}\sin\phi}{2\varepsilon_s\sqrt{S_{ij,s} : S_{ij,s} + \theta_s / d_s^2}} \tag{15}$$

where, $\varepsilon_{s,\min}$ is the minimum value of solid volume fraction above which frictional stresses are evaluated, ϕ is the angle of internal friction and $S_{ij,s}$ is the strain rate tensor for the solid phase.

The values of empirical parameters, F, a, b are taken equal to 0.05, 2, 5 as proposed by Johnson et al. (1990). The angle of internal friction is 28.5^0 as reported in Johnson et al. (1990). The value of $\varepsilon_{s,\min}$ is taken equal to 0.5 as suggested by Srivastava and Sundaresan (2003).

The frictional component of bulk viscosity, ξ_s^f is zero in the closure of Srivastava and Sundaresan (2003).

For closing the momentum balance equations, constitutive equations are also required for the gas-solid drag coefficient, Φ_{gs}. The drag model of Gidaspow (1994) is used in the present work. The constitutive equations in Gidaspow (1994) model are as follows

$$\Phi_{gs} = 150\frac{(1-\varepsilon_g)^2\mu_g}{\varepsilon_g(\psi_s d_s)^2} + 1.75\frac{\varepsilon_s\rho_g\left|\overline{U_g}-\overline{U_s}\right|}{\psi_s d_s} \qquad \varepsilon_g \le 0.8$$

$$\Phi_{gs} = \frac{3}{4}C_D\frac{\varepsilon_s\varepsilon_g}{\psi_s d_s}\rho_g\left|\overline{U_g}-\overline{U_s}\right|\varepsilon_g^{-2.65} \qquad \varepsilon_g > 0.8$$

$$C_D = \frac{24}{\mathrm{Re}_s}\left(1+0.15\mathrm{Re}_s^{0.687}\right) \quad \mathrm{Re}_s \le 1000 \qquad (16)$$

$$C_D = 0.44 \qquad \mathrm{Re}_s > 1000$$

$$\mathrm{Re}_s = \frac{\rho_g d_s\left|\overline{U_g}-\overline{U_s}\right|\varepsilon_g}{\mu_g}$$

3.3 Granular temperature equation

The granular temperature equation is the conservation equation for the kinetic energy of particles associated with their random or fluctuating motions. The equation has the following form

$$\frac{3}{2}\left[\frac{\partial}{\partial t}(\beta_v\varepsilon_s\rho_s\theta_s)+\frac{\partial}{\partial x_i}(\beta_i\varepsilon_s\rho_s U_{i,s}\theta_s)\right] = \beta_v\left(\Pi_{ij,s}^{kc}:\frac{\partial U_{j,s}}{\partial x_i}\right)+\frac{\partial}{\partial x_i}\left(\beta_i k_s\frac{\partial\theta_s}{\partial x_i}\right)-\beta_v\gamma_s-3\beta_v\Phi_{sg}\theta_s \qquad (17)$$

The two terms on left hand side represent accumulation and convection while the terms on the right hand side represent production due to shear, diffusive transport, dissipation due to inelastic collisions and dissipation due to fluid friction.

The conductivity of granular temperature, k, and collisional energy dissipation term, γ_s are expressed as

$$k_s = \frac{2k_{dil,s}}{(1+e_s)g_0}\left\{1+\frac{6}{5}(1+e_s)g_0\varepsilon_s\right\}^2 + 2\varepsilon_s^2\rho_s d_s g_0(1+e_s)\sqrt{\frac{\theta_s}{\pi}} \qquad (18)$$

$$k_{dil,s} = \frac{75}{384}\rho_s d_s\sqrt{\pi\theta_s} \qquad (19)$$

$$\gamma_s = 3(1-e_s^2)\varepsilon_s^2\rho_s g_0\theta_s\left(\frac{4}{d_s}\sqrt{\frac{\theta_s}{\pi}}-\frac{\partial U_{k,s}}{\partial x_k}\right) \qquad (20)$$

Detailed derivations of the conservation equations listed so far are present in Gidaspow (1994).

3.4 Thermal energy balance equations

The thermal energy balance equation represents the net accumulation of energy in each phase due to convection, diffusion, and interphase heat transfer. The thermal energy balances for the gas and solid phase are as follows:

Gas Phase:

$$\frac{\partial}{\partial t}\left(\beta_v \varepsilon_g \rho_g H_g\right)+\frac{\partial}{\partial x_i}\left(\beta_i \varepsilon_g \rho_g U_{i,g} H_g\right)=\frac{\partial}{\partial x_i}\left(\beta_i \varepsilon_g \kappa_g \frac{\partial T_g}{\partial x_i}\right)+\beta_v \alpha_v \left(T_s - T_g\right) \tag{21}$$

Solid Phase:

$$\frac{\partial}{\partial t}\left(\beta_v \varepsilon_s \rho_s H_s\right)+\frac{\partial}{\partial x_i}\left(\beta_i \varepsilon_s \rho_s U_{i,s} H_s\right)=\frac{\partial}{\partial x_i}\left(\beta_i \varepsilon_s \kappa_s \frac{\partial T_s}{\partial x_i}\right)+\beta_v \alpha_v \left(T_g - T_s\right) \tag{22}$$

where, H is the enthalpy, κ is the phase thermal conductivity, α_v is the interphase volumetric heat transfer coefficient, and T_g, T_s are the gas and solid phase temperature respectively.

In order to close the thermal energy balance equations, expressions for gas and solid phase thermal conductivities (κ_g and κ_s) and interphase volumetric heat transfer coefficient, α_v are required. Constitutive equations for phase thermal conductivities and the interphase volumetric heat transfer coefficient are discussed in the following subsections.

3.4.1 Constitutive equations for the thermal conductivities of phases

The phase thermal conductivities in gas-solid bulk and the near wall region can differ from the respective true thermal conductivities depending on the bed structure in the bed core and the near wall region. The bed core region and near wall region are addressed separately.

3.4.1.1 Thermal conductivities of phases in the bed core

Zehner and Schluender (1970) obtained correlation for bulk gas-solid thermal conductivity, κ_b as a function of true thermal conductivities of gas and particulate phase and the bulk

voidage in a packed bed based on a random sphere packing as

$$\frac{\kappa_b}{\kappa_{g,o}} = \left(1-\sqrt{1-\varepsilon_g}\right)+\sqrt{1-\varepsilon_g}\left(\beta A+(1-\beta)K\right) \tag{23}$$

$$K = \frac{2}{1-\frac{B}{A}}\left[\frac{A-1}{\left(1-\frac{B}{A}\right)^2}\frac{B}{A}\ln\frac{A}{B}-\frac{B-1}{1-\frac{B}{A}}-0.5(B+1)\right] \tag{24}$$

where,

$$A = \frac{\kappa_{s,o}}{\kappa_{g,o}} \tag{25}$$

$$B = 1.25\left(\frac{1-\varepsilon_g}{\varepsilon_g}\right)^{10/9} \tag{26}$$

$$\beta = 7.26\times10^{-3} \tag{27}$$

where, $\kappa_{g,o}$ and $\kappa_{s,o}$ are the true thermal conductivities of the gas and solid phase ,respectively.

For an Eulerian-Eulerian model, the bulk thermal conductivity of the bed should be separated into conductivities of the gas and solid phases. Kuipers et al. (1992) reasoned that the bulk thermal conductivity can be seen to be composed of a bulk gas conductivity and bulk solid conductivity as

$$\kappa_b = \kappa_{b,g} + \kappa_{b,s} \tag{28}$$

where, $\kappa_{b,g}$ and $\kappa_{b,s}$ are the bulk thermal conductivities of the gas and solid phase respectively and expressed as

$$\kappa_{b,g} = \left(1-\sqrt{1-\varepsilon_g}\right)\kappa_{g,o} \tag{29}$$

$$\kappa_{b,s} = \sqrt{1-\varepsilon_g}\left(\beta A+(1-\beta)K\right)\kappa_{g,o} \tag{30}$$

The phase thermal conductivities are then obtained by dividing the bulk thermal conductivity by the volume fraction of the respective phase and expressed as

$$\kappa_g = \frac{\left(1-\sqrt{1-\varepsilon_g}\right)\kappa_{g,o}}{\varepsilon_g} \tag{31}$$

$$\kappa_s = \frac{\left(\beta A+(1-\beta)K\right)\kappa_{g,o}}{\sqrt{1-\varepsilon_g}} \tag{32}$$

3.4.1.2 Thermal conductivities of phases in the near wall region

The previous studies on the numerical prediction of heat transfer coefficient between an immersed obstacle and a gas-solid fluidized bed have obtained the phase thermal conductivities in the vicinity of the heated surface from Zehner and Schluender (1970) model by using Eqs. 31 and 32. Henceforth, this approach will be called the standard approach.

It has been discussed in section 1 that the above approach applies the Zehner and Schluender (1970) thermal conductivity model developed for heat conduction in the bed core to the heat conduction in the near wall region and ignores the physical background of heat transfer to a solid assembly in contact with a heated surface. Legawiec and Ziolkowski (1994) have addressed this problem and developed a correlation where the effective or bulk thermal conductivity of the solid assembly within half a particle diameter from the wall is related to the distance l from the wall (see Figure 2), and number of particles N_p in contact with unit area of the wall as

$$\kappa_{e,s} = \frac{l N_p Q_w}{(T_w - T_s)} \tag{33}$$

where, $\kappa_{e,s}$ is the effective thermal conductivity of the solids in contact with the wall , Q_w is the rate of heat transfer from the wall to a single sphere. When, Q_w and N_p are replaced by their respective expressions given in Legawiec and Ziolkowski (1994), $\kappa_{e,s}$ for the case of a flat wall surface is obtained as

$$\kappa_{e,s} = 3\kappa_{g,o}\overline{\varepsilon_s} S\Phi \tag{34}$$

where, $\overline{\varepsilon_s}$ is the average solid volume fraction of the near wall layer of solids within a particle radius from the wall and S is the ratio of the distance from the wall to the radius of the particle expressed as

$$S = 2l / d_s \tag{35}$$

Further,

$$\Phi = \left(\frac{A}{A-1}\right)^2 \left[\left(1 - \frac{1-S}{A}\right)\ln(A) - \frac{A-1}{A}S\right] \tag{36}$$

where, A is the ratio of thermal conductivity of solid material and the fluid as described in Eq. 25. The detailed derivation of Eq. 34 is present in Legawiec and Ziolkowski (1994).

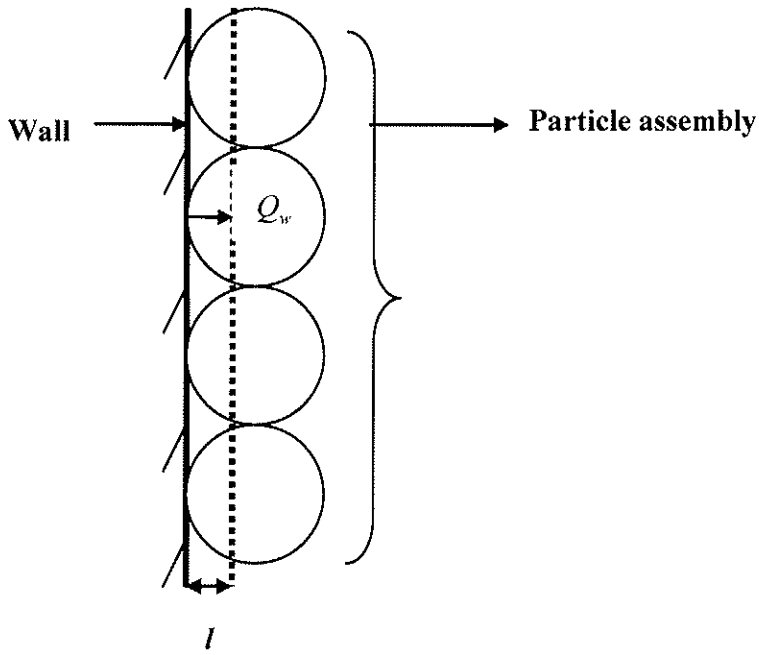

Figure 2 Schematic of particle-wall assembly used in Legawiec and Ziolkowski (1994) model

In order to assess the impact of the Legawiec and Ziolkowski (1994) model on the predicted wall to bed heat transfer coefficient, it is incorporated into the in-house code FLOTRACS-MP-3D. This model is applied only in the region within a distance equal to half a particle diameter from the wall surface (heated tube surface) as only the particles in this region can be in direct contact with the wall. The constitutive equation for the solid phase thermal conductivity is obtained by dividing the expression for effective solid phase thermal conductivity in Eq. 34 by the average solid porosity of the near wall layer of solids within a

particle radius from the wall. Similar to the solid phase, a constitutive equation for the gas phase thermal conductivity is required in the near wall region. Since the voidage in the near wall region is higher than the voidage in the bed core (Legawiec and Ziolkowsky (1994)) and heat is conducted in the gas phase through molecular conduction, the gas phase conductivity is taken equal to its true thermal conductivity in the region within half a particle diameter from the wall

The constitutive equations for the phase thermal conductivities are then expressed as

$$\left.\begin{aligned} \kappa_g &= \kappa_{g,o} \\ \kappa_s &= \kappa_{e,s} / \overline{\varepsilon_s} = 3\kappa_{g,o} S\Phi \end{aligned}\right\} \quad l/d_s \le 0.5 \tag{37}$$

Where, $\kappa_{e,s}$ is obtained from Eq. 34. The aforementioned evaluation of phase thermal conductivities will be termed as current approach here onwards. The gas and solid phase thermal conductivities in the distances exceeding half the particle diameter from the wall are still obtained from the standard approach.

3.4.2 Constitutive equation for the interphase volumetric heat transfer coefficient

The thermal energy balance equations for the gas and solid phases are connected through the volumetric interphase heat transfer coefficient, α_v which is obtained by multiplying the specific interfacial area with heat transfer coefficient between a single particle and gas as

$$\alpha_v = \frac{6\varepsilon_s \alpha_{gs}}{d_s} \tag{38}$$

where, α_{gs} is the gas-particle heat transfer coefficient and given by Gunn's (1978) correlation as

$$\begin{aligned} \frac{\alpha_{gs} d_s}{k_{g,o}} &= \left(7 - 10\varepsilon_g + 5\varepsilon_g^2\right)\left(1 + 0.7(\mathrm{Re}_s)^{0.2}(\mathrm{Pr})^{0.33}\right) \\ &+ \left(1.33 - 2.40\varepsilon_g + 1.20\varepsilon_g^2\right)(\mathrm{Re}_s)^{0.7}(\mathrm{Pr})^{0.33} \end{aligned} \tag{39}$$

where,

$$\mathrm{Pr} = \frac{\mu_g c_{p,g}}{\kappa_{g,o}} \tag{40}$$

where, $c_{p,g}$ is the specific heat of the gas phase

4. Numerical Simulations

The simulations are carried out on the finite volume in-house code FLOTRACS-MP-3D in a Cartesian coordinate system. The calculation domain is divided into control volumes. Volume fraction, pressure, turbulent kinetic energy and temperature are stored at the centre of the control volumes while velocities are stored at the surface of the control volumes. The conservation equations are integrated by a first order upwind scheme in space and a fully implicit scheme in time.

The system chosen for study is the cold pressurised laboratory scale fluidized bed used by Olsson and Almstedt (1995) to measure local instantaneous tube to bed heat transfer coefficients. Olsson and Amstedt (1995) used a 2.1 m long fluidized bed with a rectangular cross section of 0.2 m x 0.3 m. Three-dimensional numerical simulations of such a setup can be very time consuming owing to the large number of grid points required. In view of large computational effort required for three-dimensional simulations, the original rig is modelled and simulated in a two-dimensional Cartesian coordinate system. The numerical setup is 0.3 m wide and 2.1 m long. The circular tubes are treated as obstacles with square cross-sections as the in-house code is developed for cartesian coordinates. Gamwo et al. (1999) have shown that square tubes can be a reasonable approximation of circular tubes although Yurong et al. (2004) have observed that the solid phase volume fraction at the top of the tube is affected by the tube geometry.

The schematic of the numerical setup is shown in Figure 3. All the dimensions are in mm as shown in Figure 1. Heat transfer coefficients are monitored on the top, bottom and the two sides of the square obstacle in order to mimic the positions at 0, 180, 90 and 270 degrees on the circular tube in the experimental setup. It can be seen in Figure 3 that the positions chosen on the square tube can be mapped directly on to the circular tube used in the measurements.

Monosized particles of 700 microns are used in the simulations. The density, form factor, heat capacity and thermal conductivity of the particles are 2600 kg/m^3, 0.8, 840 J/Kg-K and 1.2 W/m-K respectively. The restitution coefficient is set to 0.9 as suggested by Enwald et al. (1999) for the particles used in the present study.

The initial bed height and voidage are 0.86 m and 0.46 respectively. The bed is operated at pressures of 0.1, and 1.6 MPa. The minimum fluidization velocities of the particles at the corresponding pressures are 0.42, and 0.18 m/s (Wiman and Almstedt (1997)). Two gas velocities exceeding the minimum fluidization velocity by 0.2 m/s and 0.6 m/s are used in the present work.

A very fine mesh is applied in the direction normal to the heated tube in order to capture the temperature profile in the thermal boundary layer. The smallest mesh size in the direction normal to the heated surface is 39 x 10^{-6} m which was found sufficient for a grid independent solution based on trial simulations and previous experience. The grid size increases with distance from the tube. The largest mesh size in radial and axial direction is 0.01 m.

At the inlet boundary, a plug flow condition is assumed for the entering gas. The gas phase velocity at the outlet is calculated from the total mass balance. At the outlet, volume fraction, pressure, granular kinetic energy, solid phase velocity and temperature are extrapolated from the upstream values.

At the wall surfaces, a no slip boundary condition is used for the gas phase. Particle slip at the wall is modelled from the partial slip boundary condition of Sinclair and Jackson (1989). The tube to bed local instantaneous heat transfer coefficient is defined as

$$h = \frac{\varepsilon_s \kappa_s \left|\frac{\partial T_s}{\partial x}\right| + \varepsilon_g \kappa_g \left|\frac{\partial T_g}{\partial x}\right|}{(T_w - T_b)} \tag{41}$$

where, T_w and T_b are the temperatures of the heated tube and bed bulk respectively. The heated tube is maintained at a temperature of 60 °C while the bed bulk has a temperature of 15 °C.

The time step is adjusted by an adaptive time stepping technique. The minimum and maximum time steps are $2x10^{-5}$ s and $5x10^{-6}$ s. Simulations are run for 15s of real time. Time averaged heat transfer coefficients are obtained on the last 10 s.

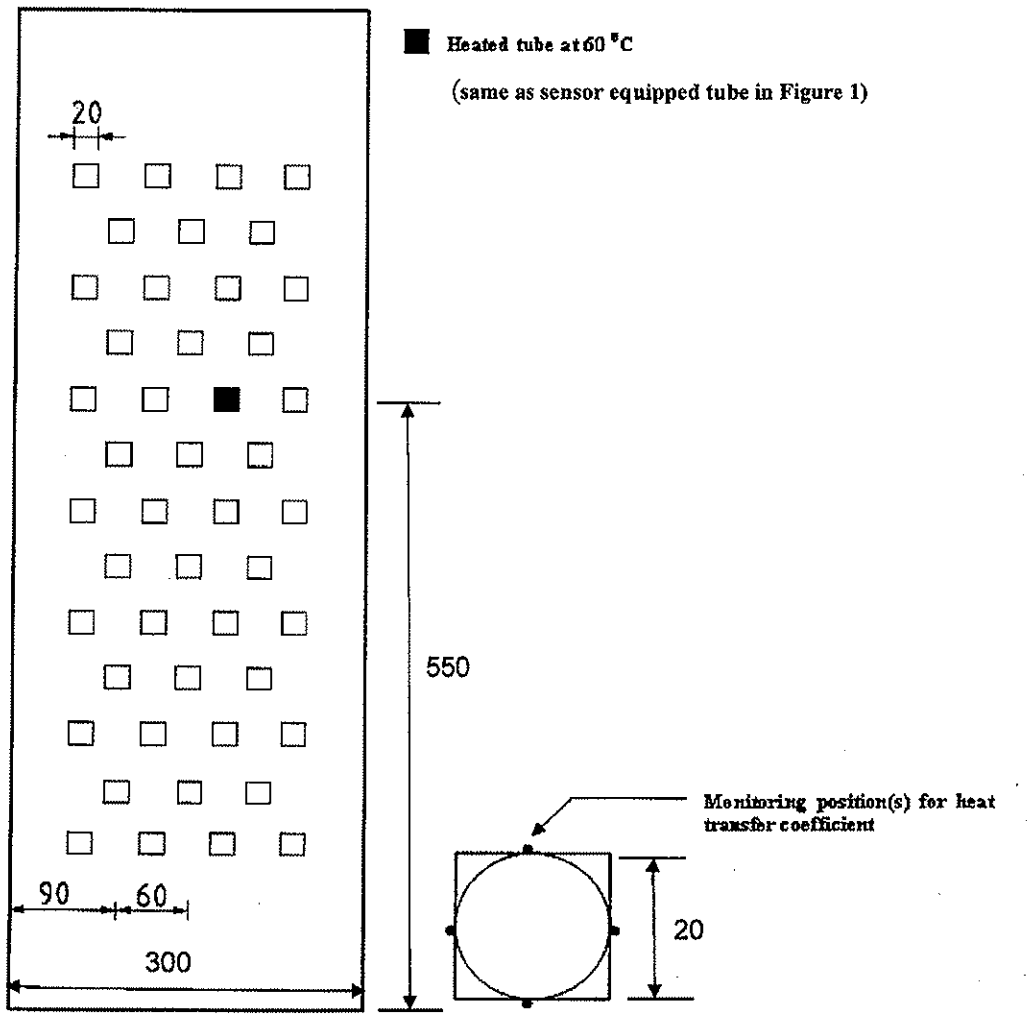

Figure 3 A schematic of S4D tube configuration with square tube geometry as incorporated into the in-house code

5. Results and Discussion

This section presents and discusses the simulation results for local instantaneous and time averaged heat transfer coefficients around the tube.

5.1 Studies on local instantaneous heat transfer coefficient around the heated tube

5.1.1 Effect of near wall phase thermal conductivity model

Figure 4 and Figure 5 show the heat transfer coefficients predicted by using the near wall phase thermal conductivity models based on the standard and current approaches outlined in section 3.4.1.2. The operating pressure and excess gas velocity are 0.1 MPa and 0.6 m/s respectively. Figure 4 corresponds to position at the top of the tube while Figure 5 corresponds to the bottom of the tube.

It is evident from Figure 4 and Figure 5 that the fluid dynamic model predicts substantially higher maxima of the heat transfer coefficient with the standard approach as compared to the current approach. The impact of phase thermal conductivity approach on the predicted heat transfer coefficient is more pronounced at the bottom of the tube where the difference in the predicted maxima from two approaches is higher than at the top. Quantitatively, the reduction in the maxima of the predicted heat transfer coefficient with the current approach as compared to the previous works of Schmidt and Renz (2005) with the standard approach is quite significant and it is important to analyse the underlying causes responsible for this reduction. It will be shown later that the lower heat transfer coefficient predicted with the current approach is in much better agreement with the measured values.

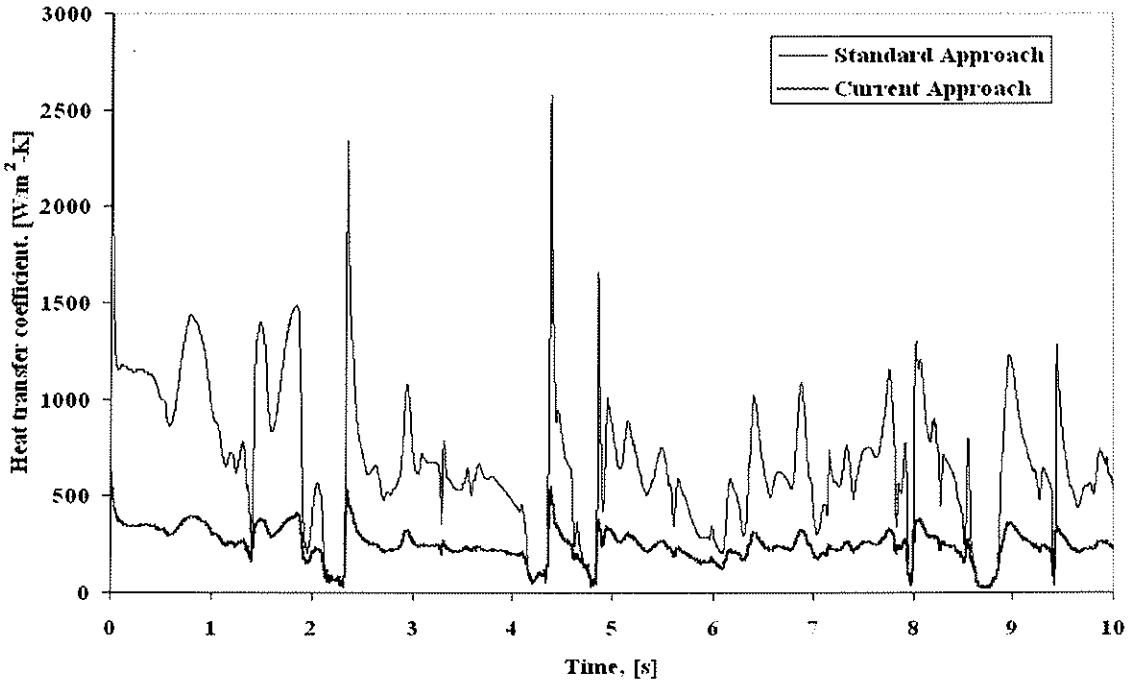

Figure 4 Influence of phase thermal conductivity model on the predicted local instantaneous heat transfer coefficient at the top of the tube (U_{fl} - U_{mf} = 0.6 m/s at 0.1 MPa)

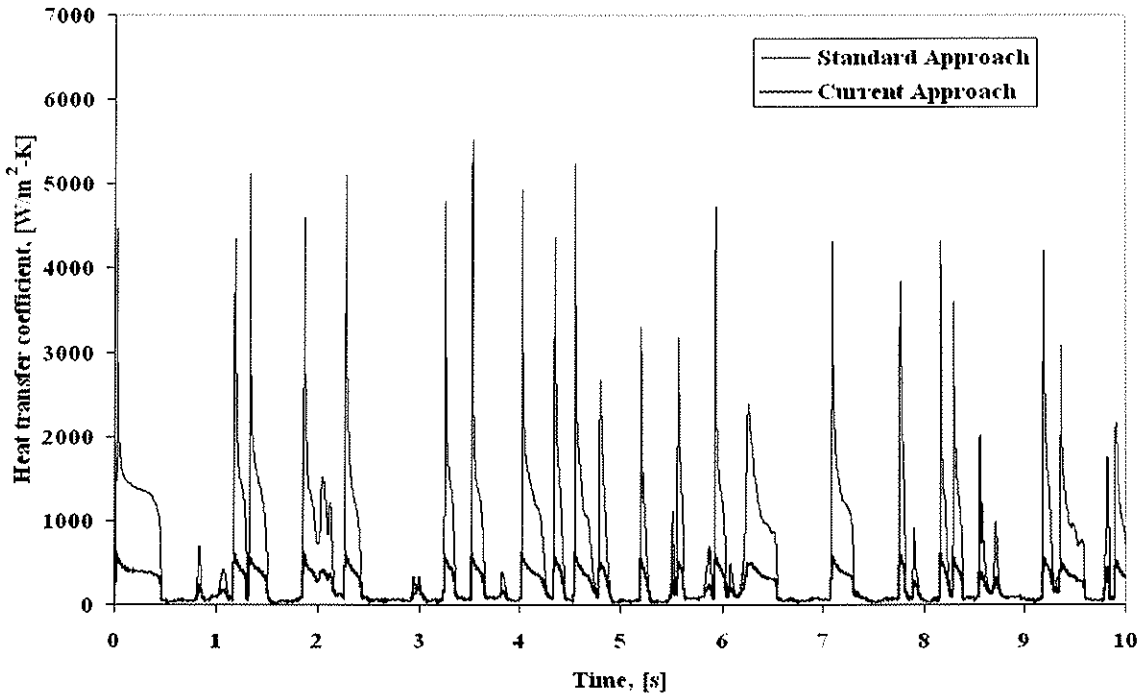

Figure 5 Influence of phase thermal conductivity model on the predicted local instantaneous heat transfer coefficient at the bottom of the tube (U_{fl} - U_{mf} = 0.6 m/s at 0.1 MPa)

In their measurements, Olsson and Almstedt (1995) have shown that the peaks of the heat transfer coefficient are nearly coincident with the peaks of the solid volume fraction. Numerical simulations mimic this trend in Figure 6 which shows the temporal variation of the local instantaneous heat transfer coefficient and solid volume fraction at the bottom of the tube. The near simultaneous occurrence of maxima of the heat transfer coefficient and the solid volume fraction implies that the maxima of heat transfer coefficient occurs due to high solid convective component of heat transfer coefficient which is a function of solid volume fraction and expressed as

$$h_s = \frac{\varepsilon_s \kappa_s \left|\frac{\partial T_s}{\partial x}\right|}{(T_w - T_b)} \tag{42}$$

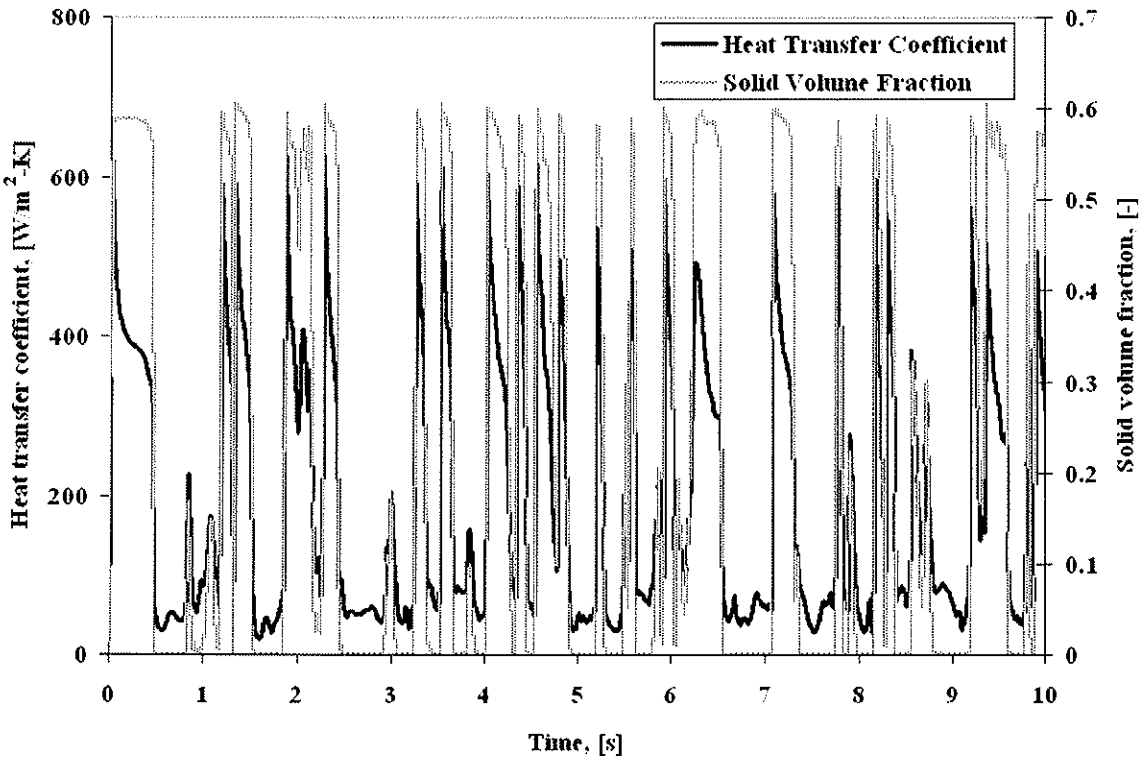

Figure 6 Temporal variation of the predicted local instantaneous heat transfer coefficient and solid volume fraction at the bottom of the tube (U_{fl} - U_{mf} = 0.6 m/s at 0.1 MPa)

Figure 7 and Figure 8 show the solid convective component of heat transfer coefficient predicted by two approaches at the top and bottom of the tube. A comparison of Figure 7 and

Figure 8 with Figure 4 and Figure 5 reveals that the quantum of difference between the maxima of the predicted solid convective component from the two approaches (Figure 7 and Figure 8) is nearly equal to the difference in maxima of the predicted total heat transfer coefficient (Figure 4 and Figure 5). This finding clearly indicates that the solid convective component is responsible for the different maxima of the total local instantaneous heat transfer coefficient obtained from the two approaches. As can be seen in Eq. 42, the solid convective component is directly proportional to solid phase thermal conductivity. The two thermal conductivity approaches investigated in the present work, namely the standard and current approach use different expressions for solid phase thermal conductivity. The different maxima of the predicted solid convective component obtained from the two approaches shows that the solid phase thermal conductivity expression is the possible reason for the observed differences.

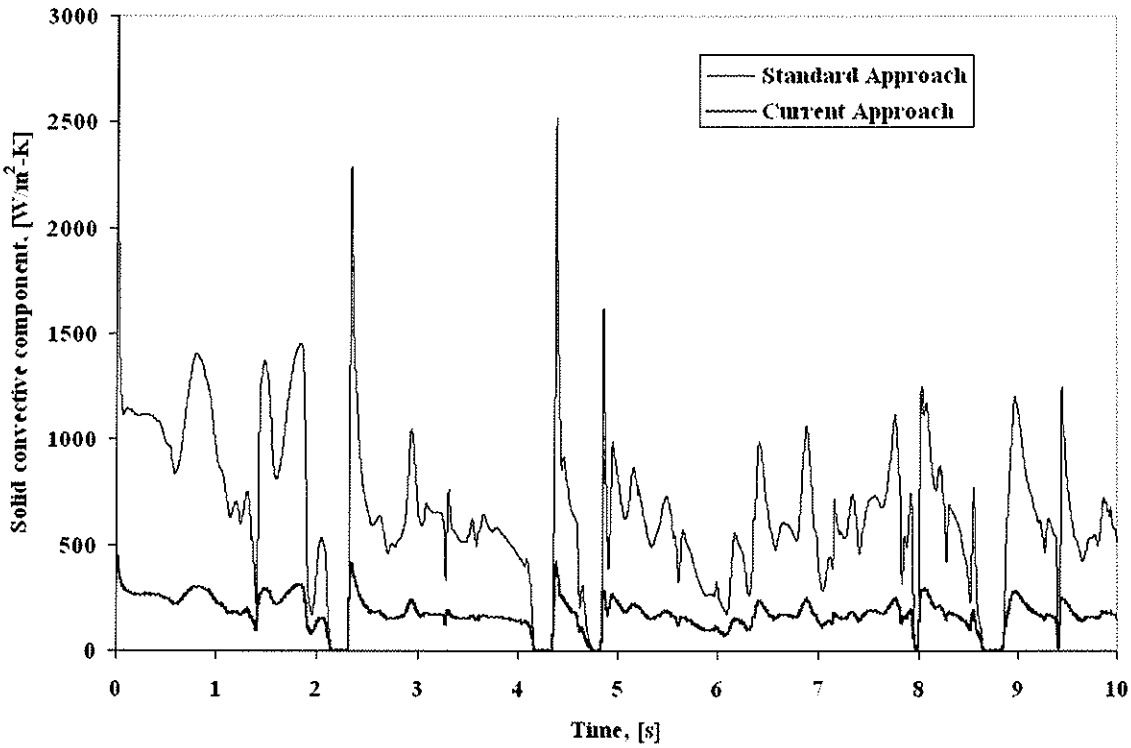

Figure 7 Temporal variation of the solid convective component of the predicted local instantaneous heat transfer coefficient at the top of the tube (U_{fl} - U_{mf} = 0.6 m/s at 0.1 MPa)

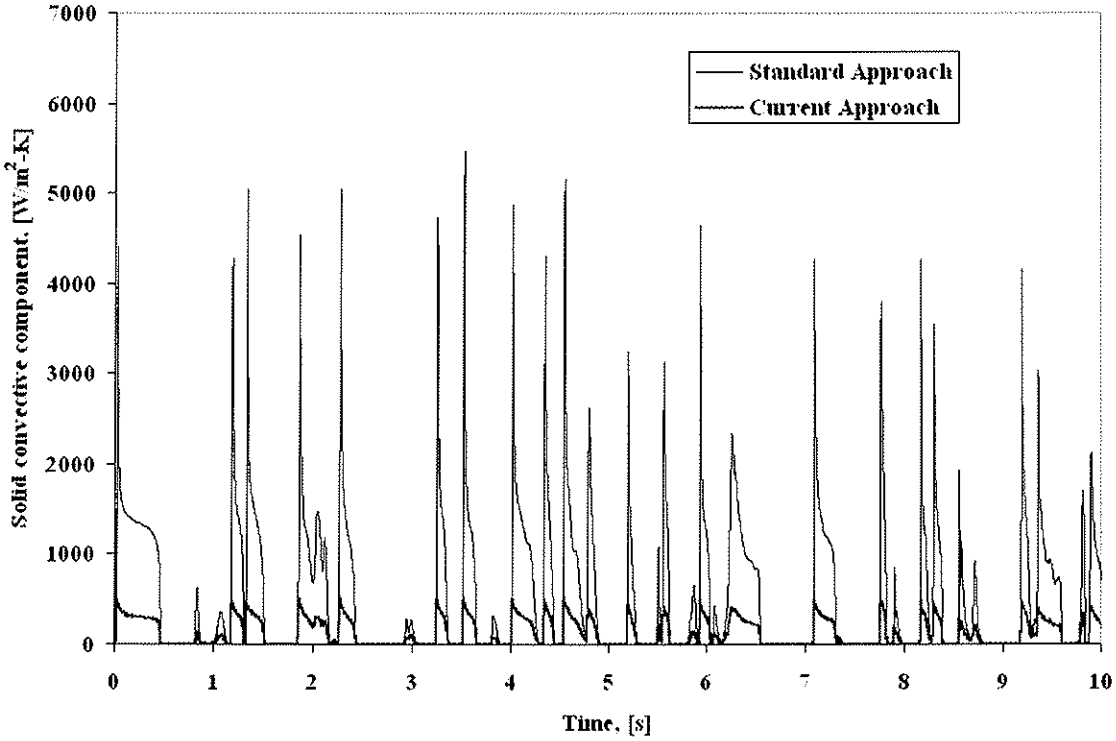

Figure 8 Temporal variation of the solid convective component of the predicted local instantaneous heat transfer coefficient at the bottom of the tube (U_{fl} - U_{mf} = 0.6 m/s at 0.1 MPa

Figure 9 plots the effective solid phase thermal conductivity computed from the two approaches as a function of local voidage for the grid point nearest to the wall ($S = 0.056$ for 700 micron particles). The current approach predicts a much lower solid phase thermal conductivity than the standard approach. The lower solid phase thermal conductivity in the current approach leads to lower maxima of the solid convective component of heat transfer which is eventually reflected in the lower maxima of the local instantaneous heat transfer coefficient predicted by the numerical model by using the current approach.

The reason for this difference in thermal conductivities computed from the two approaches can be discerned by comparing Eqs. 30 and 34 which express the effective solid phase conductivities from the standard and current approach respectively. In the standard approach based on the Zehner and Schluender (1970) model, the effective near wall thermal

conductivity of the solid phase is a function of solid porosity and the true gas and solid thermal conductivities. In the current approach based on the model of Legawiec and Ziolkowsky (1994), the effective solid thermal conductivity in the near wall region is a function of solid porosity, true gas and solid thermal conductivities and a parameter S. The parameter S is a ratio of distance from the wall and the particle size and thereby incorporates the effect of particle wall geometry on the effective solid phase thermal conductivity. Since, Zehner and Schluender (1970) model neglects this parameter, it gives a higher solid phase thermal conductivity which is based on the bed structure in the bulk of the bed.

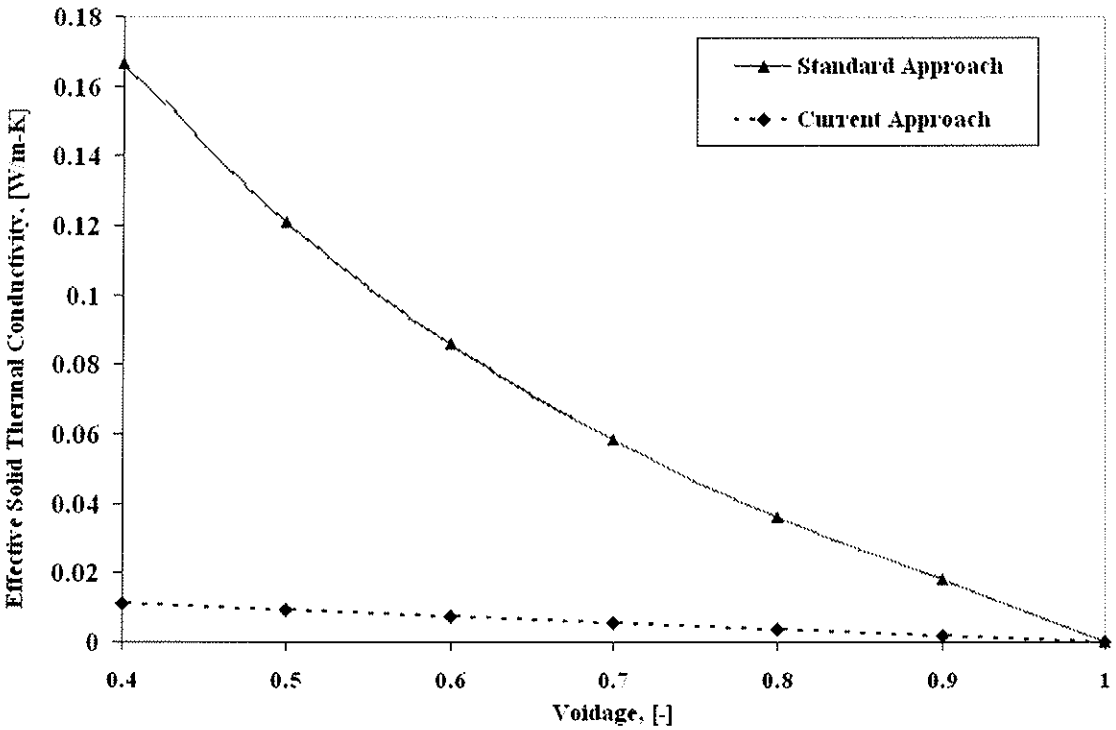

Figure 9 Variation of effective solid conductivity with local voidage

In order to assess the quantitative significance of the reduced maxima of the local instantaneous heat transfer coefficient predicted by using the current approach, a validation against measured values of the heat transfer coefficient is necessary. The measured heat transfer coefficient is constrained by the time constant of the heat flux sensor while the predictions from the numerical model are not bound by such a constraint. For obtaining meaningful comparisons, the predictions should be filtered so as to account for the time

constant of the sensor. In the present work, the filter of Roffel and Chin (1987) as suggested by Patil et al. (2006) is used. The filtered heat transfer coefficient is expressed as:

$$h_{f,n} = h_{f,n-1} e^{-\Delta t/\tau} + (1 - e^{-\Delta t/\tau}) h_{p,n} \tag{43}$$

where $h_{f,n}$ and $h_{f,n-1}$ are filtered heat transfer coefficients at instances n and n-1, Δt is the time difference between two predicted heat transfer coefficients, τ is the time constant of the sensor and $h_{p,n}$ is the predicted heat transfer coefficient at instance n. Olsson and Almstedt (1995) reported that the response time of their sensor was 50ms for a full response to a step function. In the present work, a value of 10 ms is used for the time constant of the sensor assuming a first order system. For a first order system, the full response time to a step function is equal to five times the magnitude of the time constant (Seborg et al. (2004)). Here onwards, the predicted local instantaneous heat transfer coefficient will stand for the filtered value obtained from Eq. 43 rather than the actual predicted value.

Figure 10, Figure 11, Figure 12 and Figure 13 show the predicted and measured local instantaneous heat transfer coefficients at the top and bottom of the tube for an excess gas velocity of 0.6 m/s at 0.1 MPa. Figure 10 and Figure 11 show the predicted heat transfer coefficients from both the current and standard approach.

A comparison of the predicted heat transfer coefficient (Figure 10 and Figure 11) with the measured values in Figure 12 and Figure 13 clearly shows that the standard approach used in previous works overpredicts the heat transfer coefficient. The degree of overprediction from standard approach is much higher at the bottom than at the top as observed in the previous work of Schmidt and Renz (2005) too. The predicted local instantaneous heat transfer coefficients from the current approach are in much better agreement with the measured values both at the top and bottom position of the tube. The current approach based on the thermal conductivity model of Legawiec and Ziolkowski (1994) which presents a more realistic

representation of the near wall bed structure is used in all the simulation studies reported henceforth.

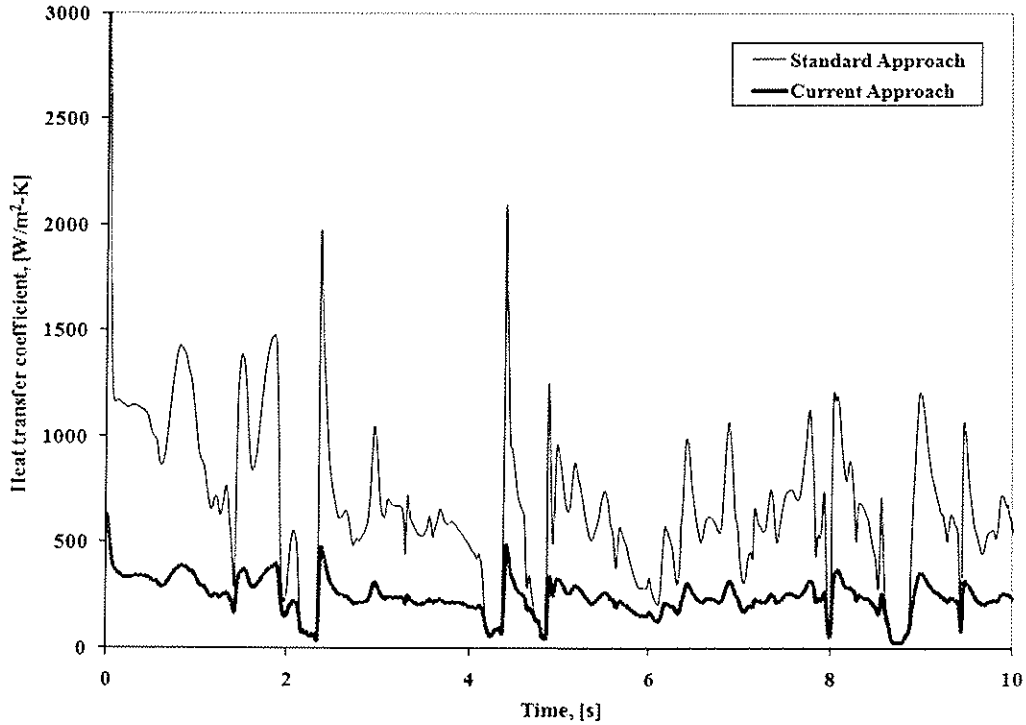

Figure 10 Temporal variation of the predicted (filtered) local instantaneous heat transfer coefficient at the top of the tube (U_{fl} - U_{mf} = 0.6 m/s at 0.1 MPa)

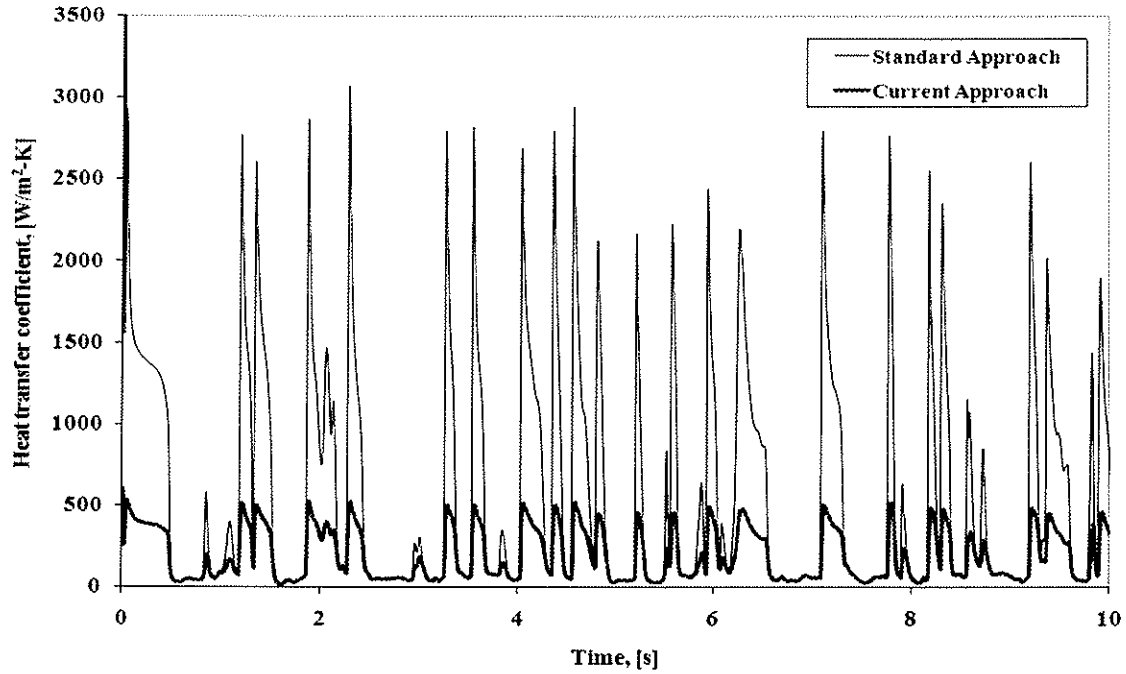

Figure 11 Temporal variation of the predicted (filtered) local instantaneous heat transfer coefficient at the bottom of the tube (U_{fl} - U_{mf} = 0.6 m/s at 0.1 MPa)

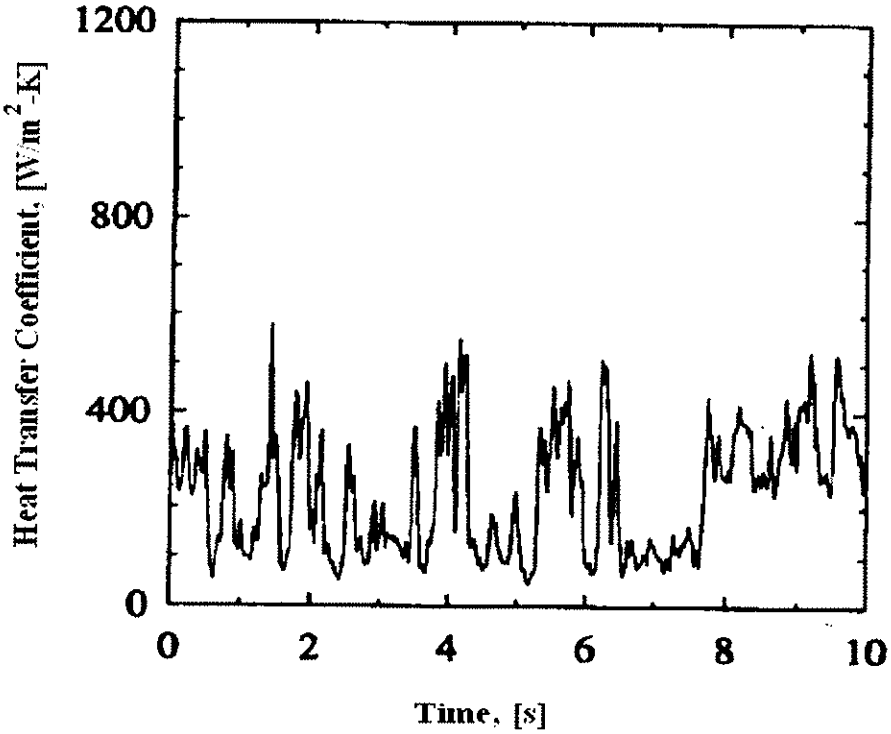

Figure 12 Temporal variation of the measured local instantaneous heat transfer coefficient at the top of the tube, U_{fl} - U_{mf} = 0.6 m/s at 0.1 MPa (Adapted from Olsson and Almstedt (1995))

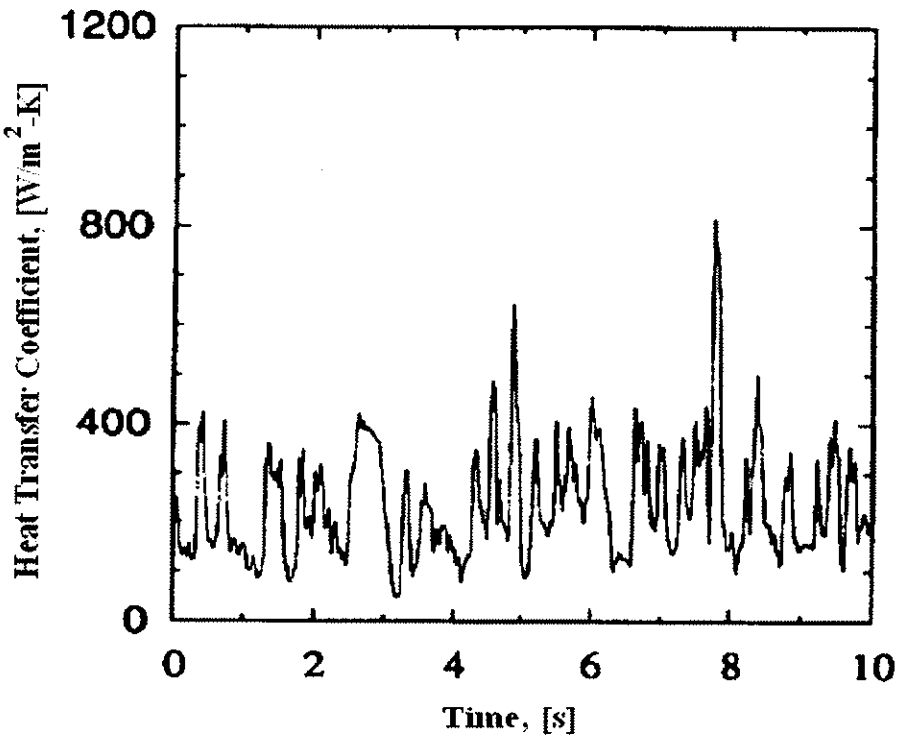

Figure 13 Temporal variation of the measured local instantaneous heat transfer coefficient at the bottom of the tube, U_{fl} - U_{mf} = 0.6 m/s at 0.1 MPa (Adapted from Olsson and Almstedt (1995))

5.1.2 Influence of operating parameters

Olsson and Almstedt (1995) have shown that the operating parameters like velocity and pressure determine the hydrodynamic behaviour around the tube and that the hydrodynamic behaviour and heat transfer around the tube are interlinked. The influence of gas fluidization velocity and pressure on the predicted local instantaneous heat transfer coefficient is analysed and compared against experimental data. Heat transfer coefficient from a heated surface to a gas-fluidized bed can be thought as a sum of a gas convective and particle convective component (Botterill, 1986). It is difficult to measure the two components separately and the numerical simulations are a useful tool which can predict the respective components separately. An analysis of the phase convective component is also presented in this section in order to gain fundamental understanding of heat transfer around obstacles in gas fluidized beds.

5.1.2.1 Effect of gas velocity

Figure 14 and Figure 15 show the predicted local instantaneous heat transfer coefficient at the top of the tube for two excess gas velocities of 0.2 m/s and 0.6 m/s at 0.1 Mpa. It should be noted that the predicted local instantaneous heat transfer coefficient at the top of the tube for the higher excess gas velocity as shown in Figure 15 has also been presented before in Figure 10 along with the predictions from the standard approach. Figure 15 shows the predictions only from the current approach in order to facilitate better visual comparison between the two excess gas velocities.

At the lower excess gas velocity, predictions in the present work (Figure 14) and measurements (Figure 16) by Olsson and Almstedt (1995) show that the heat transfer coefficient remains high barring one instance around 8-9 s when the heat transfer coefficient notches a considerably lower value as compared to other time instances when the heat transfer coefficient remains high. Such a trend is contrary to the bubbling behaviour of the bed and indicates the presence of solid phase of varying volume fractions for majority of times which

is very infrequently interrupted by a situation where solids are completely swept off the top. A look at the temporal variation of the predicted solid volume fraction at the top of the tube in Figure 17 vindicates this observation. It can be seen in Figure 17 that the solid volume fraction variation at the top of the tube does not represent a bubbling behaviour and that the dips in the predicted heat transfer coefficient coincide with the near solid free time instances at the top of the tube. The nearly identical temporal variation of local instantaneous heat transfer coefficient and solid volume fraction at the top of the tube underscores the coupling between bed hydrodynamics and heat transfer which was also observed by Olsson and Almstedt (1995) in their measurements. The numerical model is thus capable of capturing the complex transport phenomena that occurs around the tube in the fluidized bed.

At the higher excess gas velocity 0.6 m/s, predicted and measured local instantaneous heat transfer coefficient (Figure 15 and Figure 12) point to the occurrence of bubbling behaviour at the top of the tube with the heat transfer coefficient dipping to lower values (read as gas convective dominated instances) more frequently than at the lower excess gas velocity of 0. 2 m/s (Figure 14 and Figure 16). The predicted solid volume fraction at the top of the tube at the higher excess gas velocity now represents a bubbling behaviour where the frequent troughs of solid volume fraction are in fact bubbles sweeping the top of the tube (Figure 18). For a more detailed insight, Figure 19 plots the predicted gas and particle convective components at the top of the tube at an excess gas velocity of 0.6 m/s. The occurrence of bubbles (instances of low solid volume fractions) in Figure 18 is coincident with the near zero values of the solid convective component in Figure 19 when gas convection alone is present and particle convection is negligible.

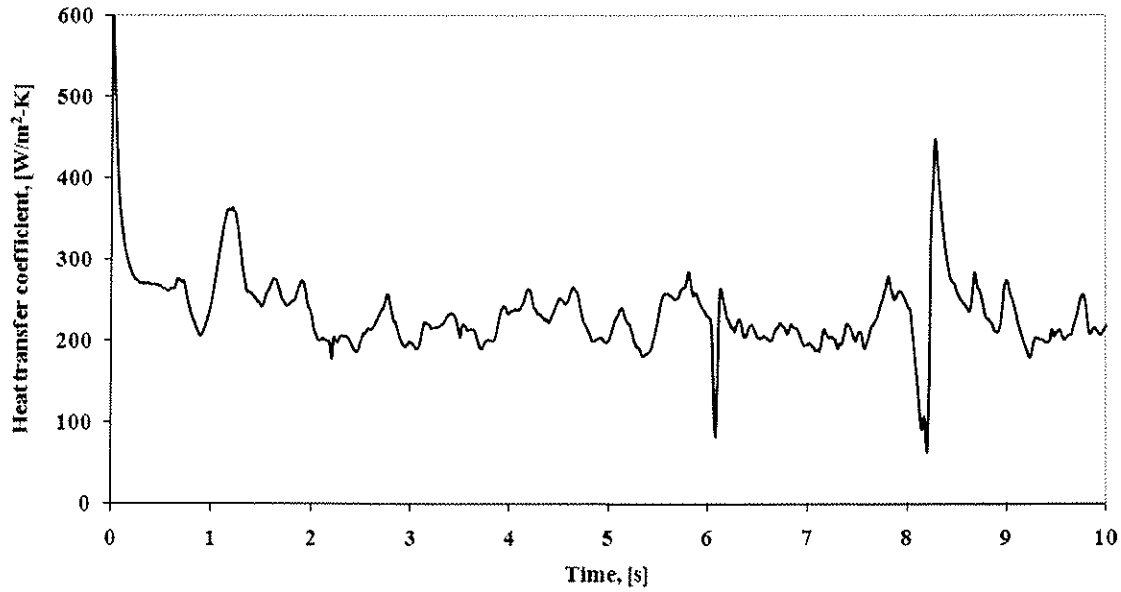

Figure 14 Temporal variation of the predicted local instantaneous heat transfer coefficient at the top of the tube (U_{fl} - U_{mf} = 0.2 m/s at 0.1 MPa)

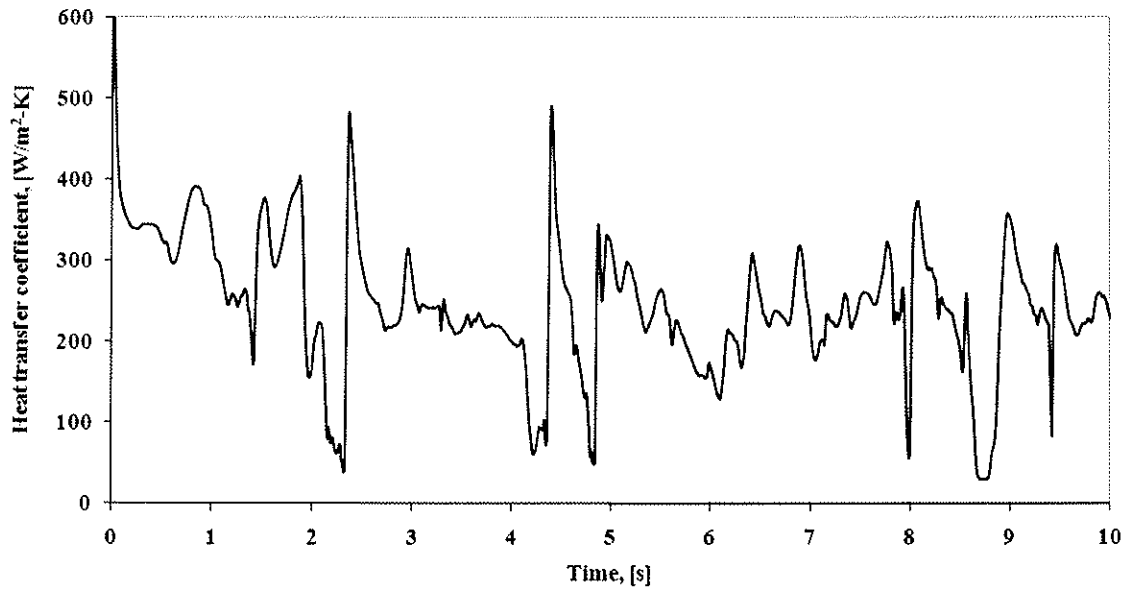

Figure 15 Temporal variation of the predicted local instantaneous heat transfer coefficient at the top of the tube (U_{fl} - U_{mf} = 0.6 m/s at 0.1 MPa)

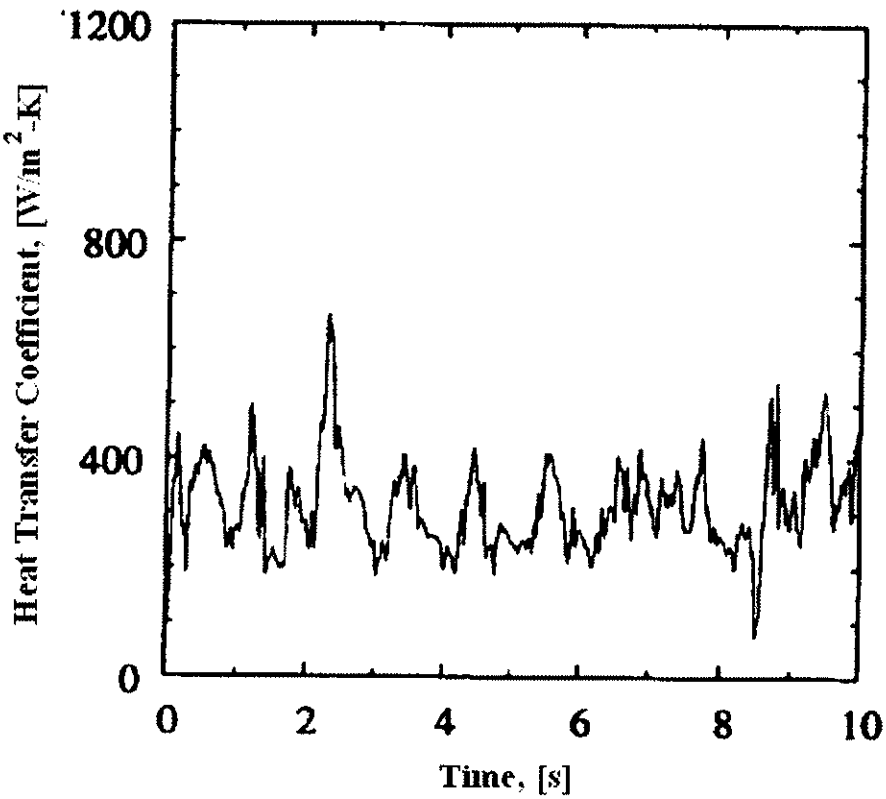

Figure 16 Temporal variation of the measured local instantaneous heat transfer coefficient at the top of the tube, U_{fl} - U_{mf} = 0.2 m/s at 0.1 MPa (Adapted from Olsson and Almstedt (1995))

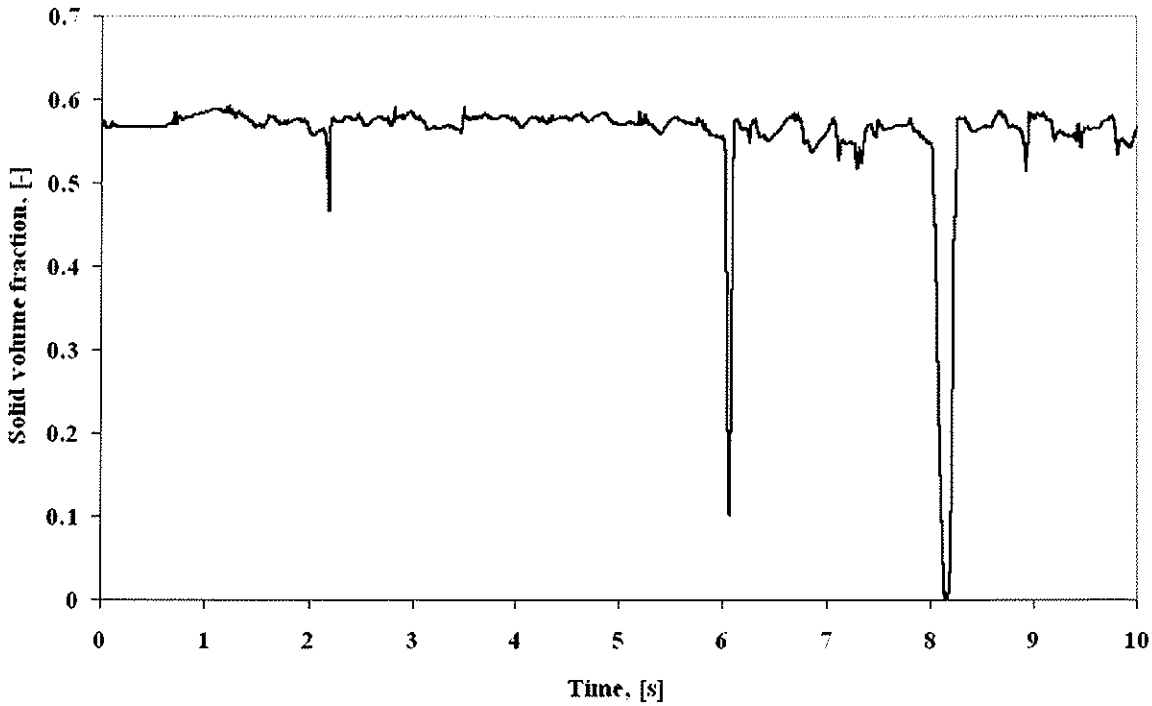

Figure 17 Temporal variation of the predicted solid volume fraction at the top of the tube (U_{fl} - U_{mf} = 0.2 m/s at 0.1 MPa)

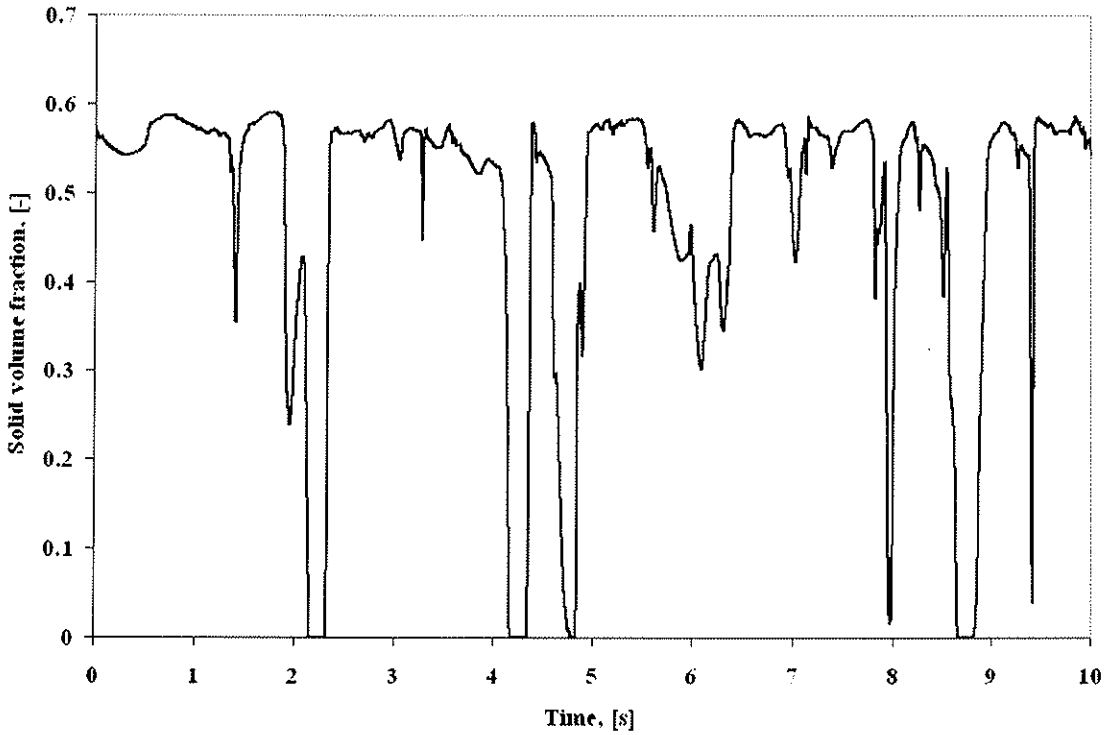

Figure 18 Temporal variation of the predicted solid volume fraction at the top of the tube (U_{fl} - U_{mf} = 0.6 m/s at 0.1 MPa)

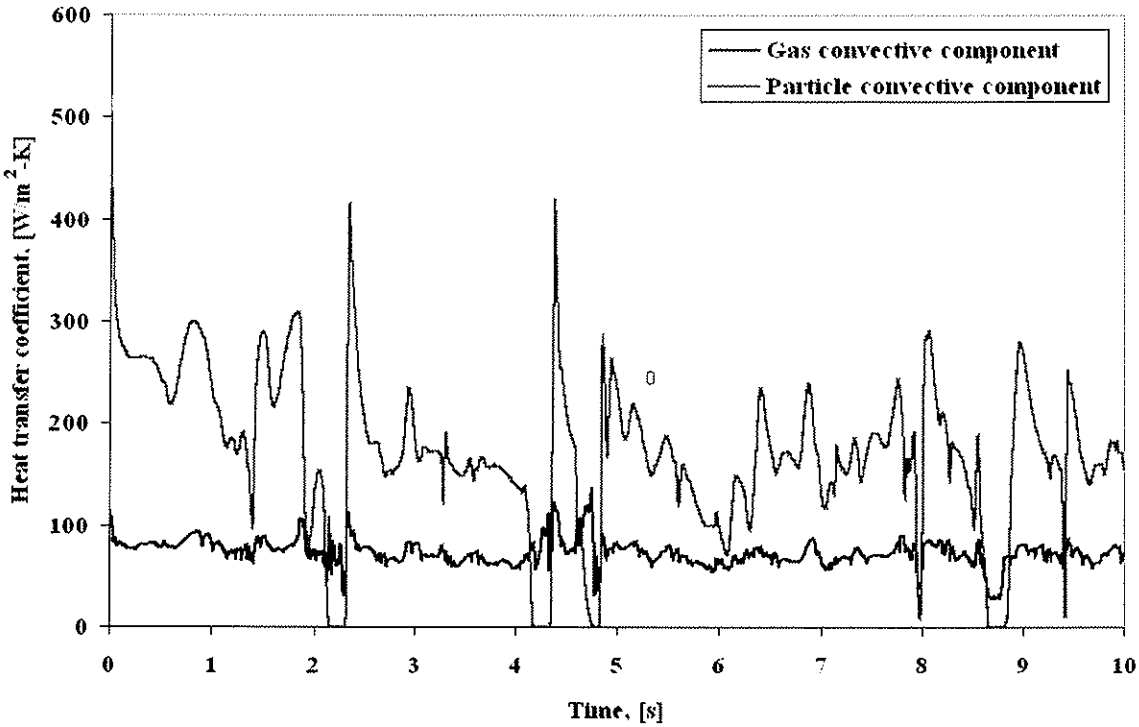

Figure 19 Temporal variation of the predicted gas and solid convective components of the local instantaneous heat transfer coefficient at the top of the tube (U_{fl} - U_{mf} = 0.6 m/s at 0.1 MPa)

5.1.2.2 Effect of operating pressure

The results on the predicted local instantaneous heat transfer coefficient presented so far have been obtained for the bed operating at atmospheric pressure (0.1 MPa) and it has been observed that the predictions at atmospheric pressure show good agreement with the measured trends reported by Olsson and Amstedt (1995). This section presents the predicted local instantaneous heat transfer coefficient around the tube for an operating pressure higher than the atmospheric pressure. The predictions are also compared against the measurements reported by Olsson et al. (1995).

Figure 20, Figure 21, Figure 22 and Figure 23 show the predicted and measured local instantaneous heat transfer coefficient on the top and bottom of the tube at an operating pressure of 1.6 Mpa for an excess gas velocity of 0.2 m/s. It can be discerned from the predicted and measured trends in Figure 20, Figure 21, Figure 22 and Figure 23 that the heat transfer coefficient at both the positions shows rapid fluctuations. Further, the maxima and minima of the heat transfer coefficient are more distinctly visible at the bottom position than at the top. The fluctuating behaviour of the local instantaneous heat transfer coefficient indicates a turbulent bed at the aforementioned operating conditions. Such a behaviour is in line with the tube erosion studies of Wiman et al. (1995) which showed a transition from bubbling to turbulent bed as the pressure was increased.

Bi and Grace (1996) have shown that increased gas density at higher pressures leads to a reduced critical gas velocity where the transition from bubbling to turbulent fluidization regime occurs. The critical gas velocity is expressed as

$$U_c = \frac{1.24\,Ar^{0.45}}{\rho_g d_s}\mu_g \tag{44}$$

Where,

$$Ar = \rho_g\left(\rho_s - \rho_g\right)d_s^3 g / \mu_g^2 \tag{45}$$

As a consequence, with increasing pressure lower superficial gas velocities are required to initiate the transition from bubbling to turbulent regime. Hence, for the same excess gas velocity, the bed is in bubbling regime at 0.1MPa but shifts to turbulent regime at higher pressure of 1.6MPa.

The transition from bubbling to turbulent regime is captured very well by the simulations as visible from Figure 24 which shows the solid volume fraction distribution inside the bed for two different pressures (0.1 MPa and 1.6 MPa) after 10 seconds of real time simulation at an excess gas velocity of 0.2 m/s. At the atmospheric pressure, the solid volume fraction distribution clearly resembles a bubbling behaviour while at the higher pressure, a turbulent behaviour comes to the fore where the solids seem to be more evenly distributed inside the bed.

The frequency of fluctuations and the magnitude of the predicted local instantaneous heat transfer coefficient are clearly under predicted in comparison to the measurements. Xie et al. (2008a, 2008b) have illustrated that differences between two and three-dimensional simulations are much higher for turbulent beds than for bubbling beds as the non-axial terms in the conservation equations become important in the turbulent regime due to increased gas velocity. The use of a two-dimensional simulation setup could be a possible cause for the discrepancies between predictions and measurements at higher pressure since the bed is in a turbulent regime. However, in the present case, it seems that the non-axial terms become important due to increased gas density at higher pressure since the transition to turbulent regime happens due to increased pressure and not increased velocity. Gas turbulence which has been excluded in the fluid dynamic model could be another factor that contributes to the high fluctuating frequency and magnitude of local instantaneous heat transfer coefficient in the measurements at 1.6 MPa.

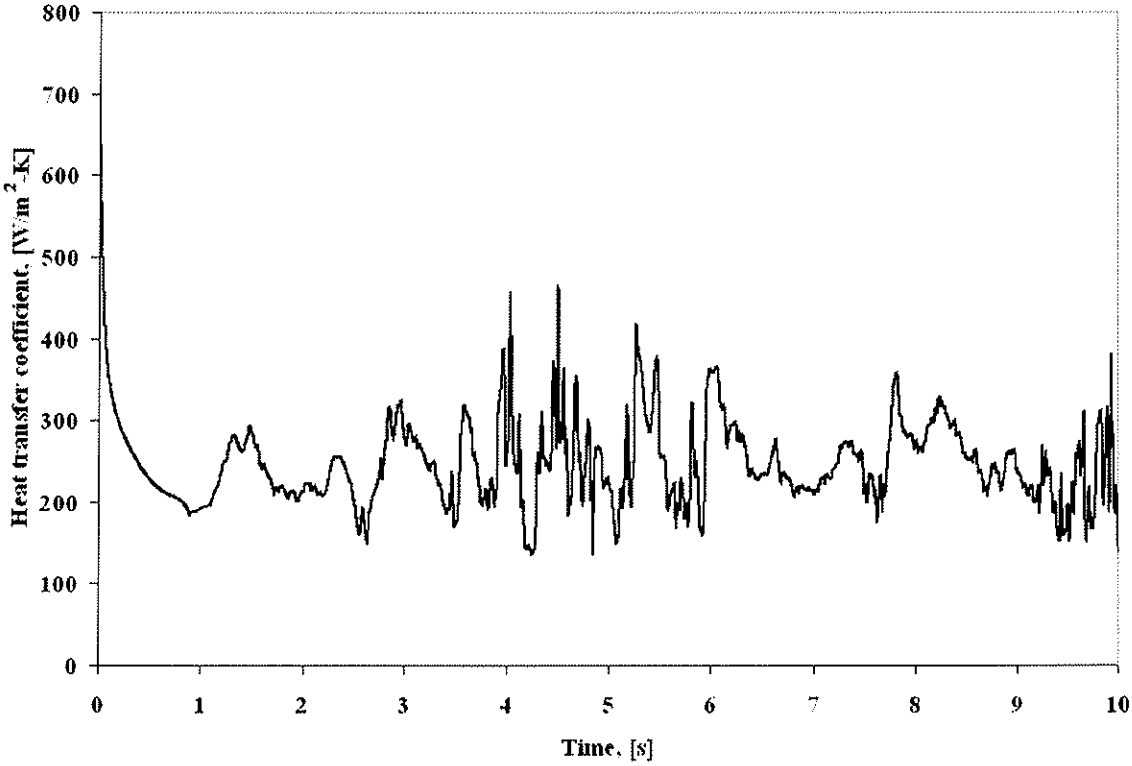

Figure 20 Temporal variation of the predicted local instantaneous heat transfer coefficient at the top of the tube (U_{fl} - U_{mf} = 0.2 m/s at 1.6 MPa)

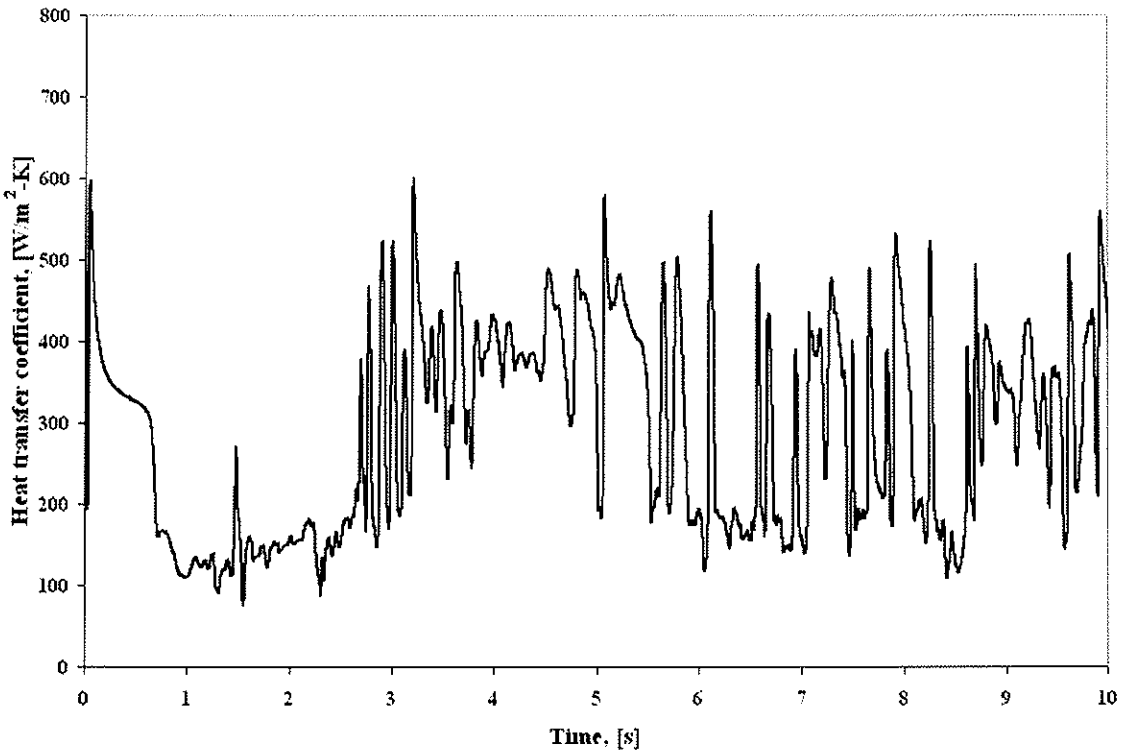

Figure 21 Temporal variation of the predicted local instantaneous heat transfer coefficient at the bottom of the tube (U_{fl} - U_{mf} = 0.2 m/s at 1.6 MPa)

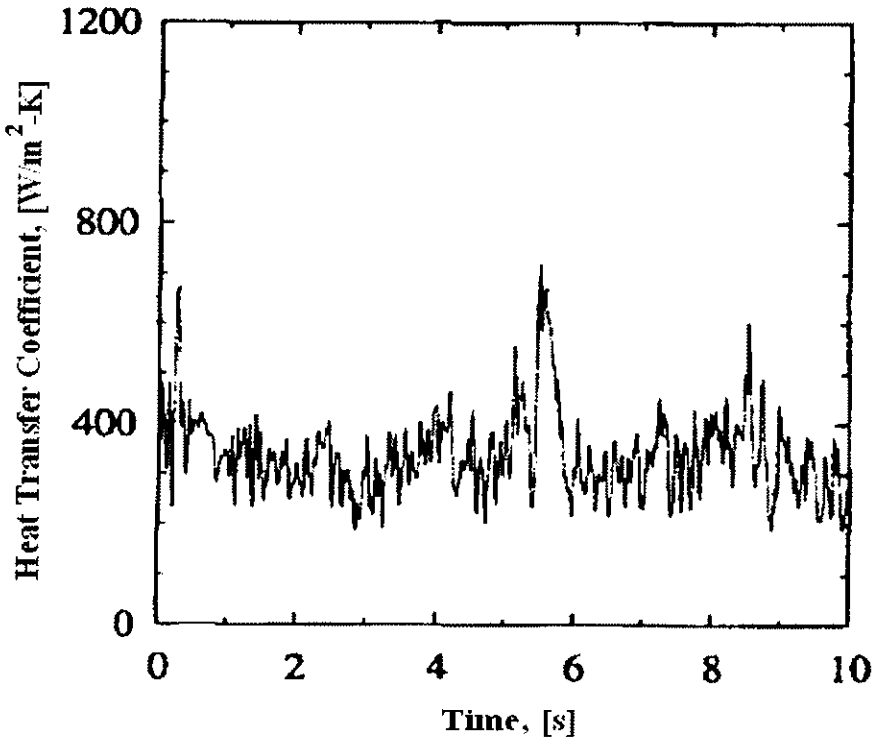

Figure 22 Temporal variation of the measured local instantaneous heat transfer coefficient at the top of the tube, U_{fl} - U_{mf} = 0.2 m/s at 1.6 MPa (Adapted from Olsson and Almstedt (1995))

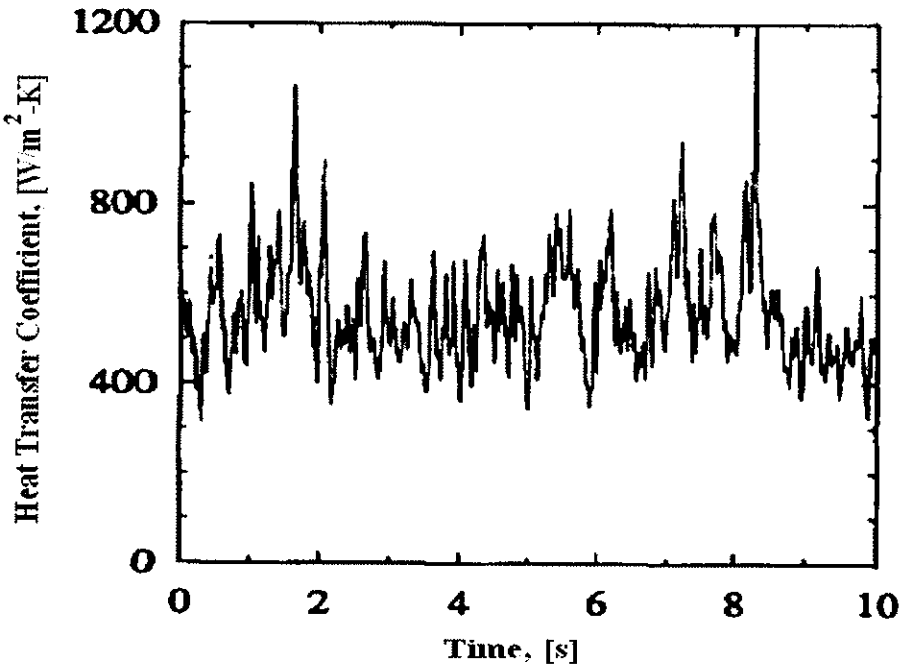

Figure 23 Temporal variation of the measured local instantaneous heat transfer coefficient at the bottom of the tube, U_{fl} - U_{mf} = 0.2 m/s at 1.6 MPa (Adapted from Olsson and Almstedt (1995))

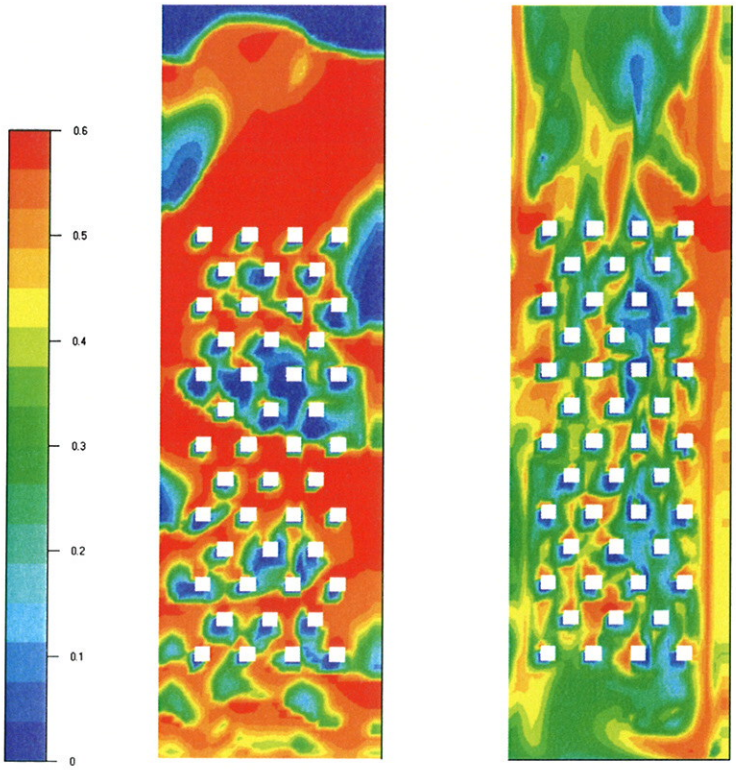

Figure 24 Snapshot of the predicted solid volume fraction distribution inside the bed after 10 seconds at two operating pressures: a) 0.1 MPa and b) 1.6 MPa (U_{fl} - U_{mf} =0.2 m/s)

Olsson and Almstedt (1995) have remarked that the most consistent and prominent trend of their experimental study is the increase of the gas convective component with increasing pressure. The reason for the increase in gas convective component lies mainly in the increased gas density and turbulent bed behaviour at higher pressure which has a favourable influence on the capacity of the gas to remove heat from the heated tube (Wiman and Almstedt (1997)). Figure 25 shows the predicted local instantaneous gas convective component at the bottom of the tube at 0.1 and 1.6 MPa. The predicted trends clearly show an increase in the gas convective component of heat transfer coefficient with increasing pressure and are well in accordance with the experimental observation of Olsson and Almstedt (1995). The qualitative effect of pressure on the heat transfer in a fluidized bed with immersed tubes is hence captured remarkably well by the numerical model.

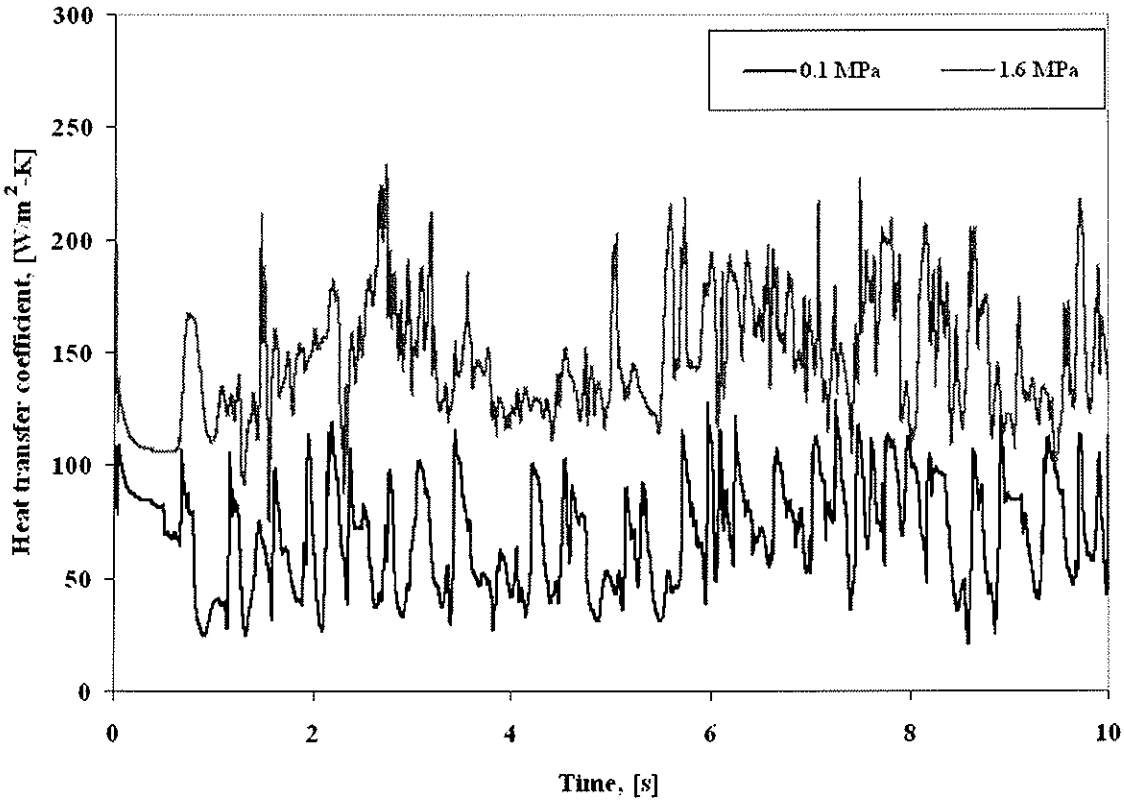

Figure 25 Effect of operating pressure on the gas convective component of the predicted local instantaneous heat transfer coefficient at the bottom of the tube (U_{ft} - U_{mf} = 0.2 m/s)

5.2 Studies on local time averaged heat transfer coefficient around the tube

Olsson and Almstedt (1995) reported local time averaged heat transfer coefficients for 12 positions on the circular tube. The local time averaged heat transfer coefficients were obtained over a 4 minute time interval. In order to compare the predictions against measurements, four positions from the circular tube at 0, 90, 180 and 270 degree are chosen. As mentioned earlier, the aforementioned positions possess identical locations on the simulated (square) and actual (circular) tube geometry where 0 and 180 degrees correspond to tube top and bottom respectively. In the figures to follow, the positions on the square tube are also shown in degrees in order to facilitate easy comparison between predictions and measurements. The local time averaged heat transfer coefficients in numerical simulations are obtained over the last 10 seconds in a simulation for 15 seconds of real time.

Figure 26 shows the predicted and measured local averaged heat transfer coefficients for four different positions on the heated tube at 0.1 Mpa and excess gas velocity of 0.6 m/s. It is evident from the figure that qualitatively the predictions are similar to the measurements. However, the predictions present a noticeable difference in the magnitude of heat transfer coefficient around the tube in comparison to measurements where a fairly constant heat transfer coefficient is observed around the tube. Quantitatively, the predictions show fair agreement with the measurements at all positions with a maximum deviation of 20% at the bottom of the tube (180 degree position). At other positions, the predicted heat transfer coefficients are within 10% of the measured values. The differences observed in the predictions and measurements could possibly be caused by two dimensional geometry, lower averaging times and square tube geometry used in the simulations.

Interestingly, the predicted time averaged heat transfer coefficient is lower than the measured values at all the positions except at the top of the tube. The increased heat transfer at the top of the tube as seen in the simulations seems to confirm the observation of Yurong et al. (2004) that the square tube geometry causes a higher concentration of particles on the top of the tube as compared to tubes with circular cross section. The increased particle concentration in turn leads to higher heat transfer at the top for tubes with square cross section due to high heat capacity of solids. Also, the high particulate concentration for square tubes seems to offset the lack of third dimension and lower averaging times in numerical simulations which is visible in the excellent agreement between predicted and measured heat transfer coefficient at the top of the tube.

The fair quantum of agreement between the predictions and measurements at the atmospheric pressure where the bed is in bubbling regime indicate that the two dimensional setup used in the numerical simulations can satisfactorily represent the three dimensional setup. These results are in accordance with the study of Xie et al. (2008a, 2008b) who carried out a detailed

budgetary analysis of 2D and 3D simulations and found good agreement between 2D and 3D simulations of bubbling beds hydrodynamics.

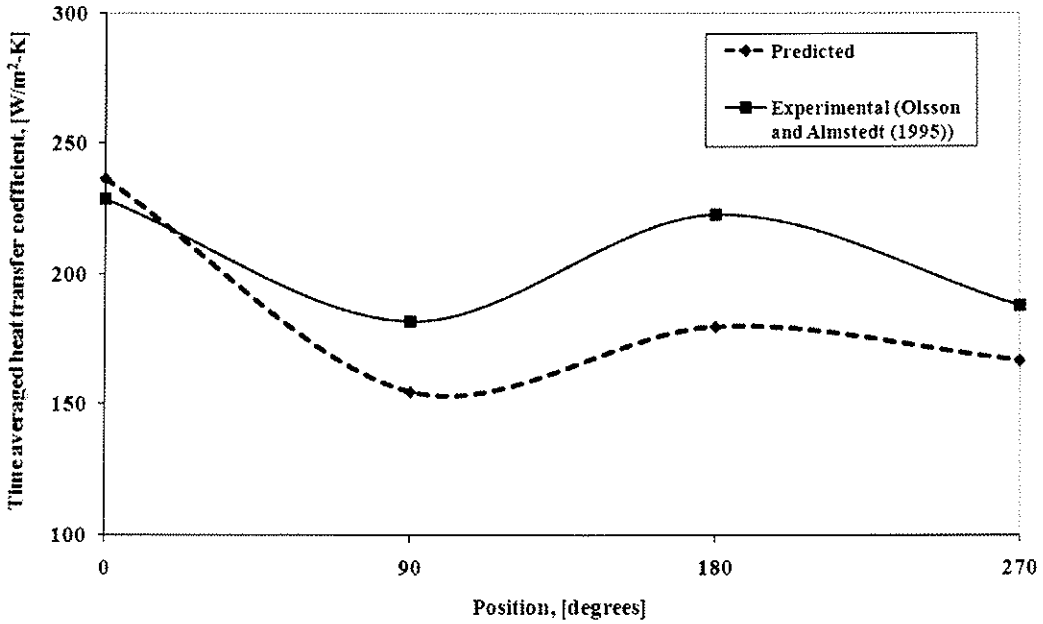

Figure 26 Comparison of the predicted and measured local time averaged heat transfer coefficients at different positions around the heated tube (U_{fl} - U_{mf} = 0.6 m/s at 0.1 MPa)

Figure 27 shows the predicted and measured local averaged heat transfer coefficients for four different positions on the heated tube at 1.6 MPa and excess gas velocity of 0.2 m/s. At this operating pressure, the predictions and measurements are similar in the respect that the highest value of heat transfer coefficient occurs at the bottom of the tube. The time averaged heat transfer coefficients are higher than the corresponding values at atmospheric pressure (Figure 26) mainly due to increased gas convective components at higher pressures. Quantitatively, predictions are under predicted as compared to measurements. It has been discussed in the studies on local instantaneous heat transfer coefficient that the under predictions possibly results from two dimensional setup and the exclusion of gas turbulence. Similar to the time averaged results at atmospheric pressure (Figure 26), the best agreement occurs at the top of the tube which again seems to happen as a result of high concentration of

the solid particles at the top of the square tubes. The increased heat capacity of solids at the top in a way compensates the heat transfer in the non-existent third dimension.

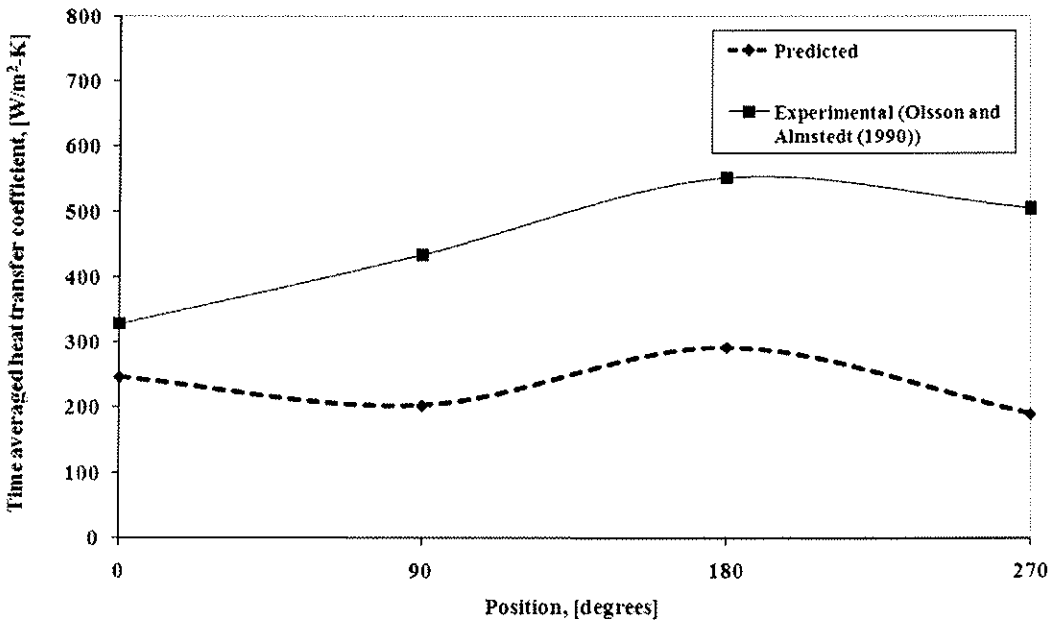

Figure 27 Comparison of the predicted and measured local time averaged heat transfer coefficients at different positions around the heated tube (U_{ft} - U_{mf} = 0.2 m/s at 1.6 MPa)

6. Conclusions

A two dimensional Eulerian-Eulerian simulation of heat transfer from an immersed tube bundle to a gas-solid fluidized bed is presented in this study. It is concluded that a realistic prediction of the local instantaneous heat transfer coefficient is subject to the constitutive equation for solid phase thermal conductivity in the near wall region. The modelling approach for solid phase thermal conductivity adopted in previous works (standard approach) over predicts the local instantaneous heat transfer coefficient around the tube. The approach of Legawiec and Ziolkowski (1994) which presents a fundamental expression for solid phase thermal conductivity in the vicinity of a wall surface is adopted in the present work (current approach).

The predicted local instantaneous heat transfer coefficient from the current approach is in better agreement with the measured values as compared to the predictions obtained by using the standard approach. The better agreement with the measured values as obtained from the current approach is due to the lower value of thermal conductivity of the solid phase which results from the inclusion of a near wall geometry parameter in the solid phase thermal conductivity model.

A strong coupling is seen between the hydrodynamics and predicted local instantaneous heat transfer coefficient around the tube as the peaks of heat transfer coefficient are nearly coincident with the high particulate concentrations.

At the atmospheric pressure, the predicted local instantaneous heat transfer coefficient at the top of the tube is strongly affected by the gas velocity in accordance with the experimental observations of Olsson and Almstedt (1995) due to increase in particle convection at higher velocity which eventually affects the total heat transfer coefficient. Both qualitatively and quantitatively, the effect of gas velocity on the top of the tube is captured well by the numerical simulations. At the lower gas velocity, the trend of local instantaneous heat transfer coefficient represents stagnation of solid phase at the top of the tube. The solids stay at the top of the tube for long time intervals which are separated by an instance of solids free period. At the higher gas velocity, the trend of the local instantaneous heat transfer coefficient represents a bubbling behaviour as the heat transfer coefficient frequently oscillates between a distinctly visible maxima and minima.

At the higher pressure of 1.6 MPa, the predicted local instantaneous heat transfer coefficient shows a fluctuating behaviour indicating the transition of the bed to a turbulent regime as observed in the experimental studies reported in literature. The transition occurs due to increased gas density at higher pressure which reduces the critical gas velocity which indicates the transition point (Bi and Grace (1996)). As a consequence, with increasing

pressure lower superficial gas velocities are required to initiate the transition from bubbling to turbulent regime. Hence, for the same excess gas velocity, the bed is in bubbling regime at 0.1MPa but shifts to turbulent regime at higher pressure of 1.6MPa

The frequency of fluctuations and the magnitude of the predicted local instantaneous heat transfer coefficient are clearly under predicted in comparison to the measurements. Xie et al. (2008a, 2008b) have illustrated that differences between two and three dimensional simulations are much higher for turbulent beds than for bubbling beds as the non-axial terms in the conservation equations become important in the turbulent regime due to increased gas velocity. The use of a two-dimensional simulation setup could be a possible cause for the discrepancies between predictions and measurements at higher pressure since the bed is in a turbulent regime. However, in the present case, it seems that the non-axial terms become important due to increased gas density at higher pressure since the transition to turbulent regime happens due to increased pressure and not increased velocity. Gas turbulence which has been excluded in the fluid dynamic model could be another factor that contributes to the high fluctuating frequency and magnitude of local instantaneous heat transfer coefficient in the measurements at 1.6 MPa.

The time averaged heat transfer coefficients around the tube are in good agreement with the measured values at the atmospheric pressure. The effect of square tube is evident as the higher concentration of solids at the top of the square tube results in a higher value of the predicted time averaged heat transfer coefficient at the top of the tube as compared to the measurements. At the higher pressure, the time averaged heat transfer coefficients are under predicted at all positions around the tube. The under prediction possibly results from the two-dimensional set up, lower averaging times and exclusion of gas turbulence.

In general it can be concluded that at the atmospheric pressure when the bed is in bubbling regime, a two-dimensional simulation with square tubes can satisfactorily predict heat transfer

for a three-dimensional fluidized bed with circular tubes. At higher pressures, the two dimensional simulation captures the qualitative trends of heat transfer coefficient but predicts lower quantitative values. To the best of authors' knowledge, this was the first study on numerical simulation of heat transfer from a tube bundle in a pressurised fluidized bed and a full three dimensional simulation at high pressures is recommended as a future work.

Nomenclature

c_p	specific heat, J/kg
d_s	diameter of solid particle, m
e_s	coefficient of restitution for particle-particle collisions
e_w	coefficient of restitution for particle-wall collisions
g_0	radial distribution function for solid phase
g_j	j direction component of gravity, m/s^2
H	enthalpy, J/kg
h	local instantaneous heat transfer coefficient, W/m^2-K
k	granular conductivity of solid phase, kg/m-s
l	distance from the wall, m
l_f	thickness of gas film between the wall and particles, m
N_p	number of particles in contact with unit area of the wall
P	fluid pressure, N/m^2
P_c	critical state pressure, N/m^2
P_s	solid phase pressure, N/m^2
Q_w	rate of heat transfer from the wall to a single particle, W
S	ratio of distance from the wall to particle radius

S_{ij}	strain rate tensor, 1/s
t	time, s
T	temperature, K
T_b	temperature of the bed bulk, K
T_w	temperature of the heated tube, K
$\overline{U}$	mean velocity, m/s
U_c	critical gas velocity, m/s
U_{fl}	superficial fluidization velocity, m/s
U_{mf}	minimum fluidization velocity, m/s
$U_{fl} - U_{mf}$	excess gas velocity, m/s
$U_{i,j}$	i, j components of velocity, m/s
x_i	coordinate in i direction, m

Greek Symbols

α_{gs}	heat transfer coefficient between a single particle and gas, W/m^2-K
α_v	interphase volumetric heat transfer coefficient between gas and solid phase, W/m^3-K
β_v	volume porosity
β_i	area porosity in i direction
ε	volume fraction
$\varepsilon_{s,\max}$	solid volume fraction at maximum packing
$\overline{\varepsilon}_s$	average solid porosity within half a particle radius distance from the wall

surface

$\Pi_{ij,s}$ total stress tensor, solid phase, N/m^2

κ thermal conductivity, W/m-K

$\kappa_{e,s}$ effective thermal conductivity of solids, W/m-K

κ_b thermal conductivity of the gas-solid bulk in a packed bed, W/m-K

$\kappa_{b,g}$ bulk thermal conductivity of gas phase, W/m-K

$\kappa_{b,s}$ bulk thermal conductivity of solid phase, W/m-K

$\kappa_{g,o}$ true thermal conductivity of gas phase, W/m-K

$\kappa_{s,o}$ true thermal conductivity of solid particles, W/m-K

μ_g laminar viscosity of the gas phase, kg/m-s

μ_s shear viscosity of solid phase, kg/m-s

δ_{ij} kronecker delta

ρ density, kg/m^3

ψ_s form factor for solid phase

ξ_s solid phase bulk viscosity, kg/m-s

$\tau_{ij,g}$ gas phase stress tensor, N/m^2

θ_s granular temperature of solid phase s, m^2/s^2

ϕ angle of internal friction

γ collisional dissipation of energy, kg/m^3-s

ρ_g gas density, kg/m^3

ρ_s solid density , kg/m^3

Φ_{gs} gas-solids drag coefficient, kg/m^3-s

Subscripts

b	bulk
g	gas
i, j, k	directions of velocity
s	solid

Superscripts

f	frictional component
kc	kinetic collisional component

Dimensionless Numbers

Ar	Archimedes number, $\rho_g\left(\rho_s-\rho_g\right)d_s^3 g/\mu_g^2$
Pr	Prandtl Number, $\frac{\mu_g c_{p,g}}{\kappa_{g,o}}$
Re_s	Particle Reynold's Number, $\frac{\rho_g d_s\left\|\overline{U}_g-\overline{U}_s\right\|\varepsilon_g}{\mu_g}$

References

1. Bi, H. T., and Grace, J. R., 1996, Effects of pressure and temperature on flow regimes in gas-solid fluidization systems, *Can. J. Chem Eng.*, 74, 1025-1027
2. Botterill, J.S.M., 1986, Gas Fluidization Technology (Ed. Geldart, D.), Wiley, Chichester
3. Enwald, H., Peirano, E., Almstedt, A.E., and Leckner, B., 1999. Simulation of the fluid dynamics of a bubbling fluidized bed. Experimental validation of the two-fluid model and evaluation of a parallel multiblock solver, *Chem. Engng. Sci.*, 54, 311-328
4. Gamwo, I.K., Soong, Y., and Lyczkowski, R.W., 1999. Numerical simulation and experimental validation of solids flow in a bubbling fluidized bed, *Powder Technol.*, 103, 117-129

5. Gidaspow, D., 1994. Multiphase Flow and Fluidization: Continuum and Kinetic Theory Descriptions, Academic Press
6. Gunn, D J., 1978. Transfer of heat or mass to particles in fixed and fluidized beds", *Int. J. Heat Mass Transfer*, 21, 467-476
7. Johnson, P.C., and Jackson, R., 1987. Frictional-collisional constitutive relations for granular materials with applications to plane shearing, *J. Fluid Mech.*, 176, 67-93
8. Johnson, P.C., Nott, P., and Jackson, R., 1990. Frictional-collisional equations of motions for particulate flows and their application to chutes, *J. Fluid mechanics*, 210, 501-535
9. Kuipers, J.A.M., Prins, W., and van Swaaij, W.P.M., 1992. Numerical calculation of wall to bed heat transfer coefficients in gas fluidized beds, *AIChE J.*, 38, 1079-1091
10. Legawiec, B. and Ziolkowski, D., 1994. Structure, voidage, and effective thermal conductivity of solids within near-wall region of beds packed with spherical pellets in tubes, *Chem. Engng. Sci.*, 49, 2513-2520
11. Ma, D., and Ahmadi, G., 1986. An equation of state for dense, rigid gas spheres, *J. Chem. Phys.*, 84, 3449-3450
12. Mathiesen, V., Arastoopur, H. and Hjertager, B.H., 1999. Experimental and computational study of multiphase gas/particle flow in a CFB riser, *AIChE J.*, 45, 2503-2518
13. Mathiesen, V., Solberg, T., and Hjertager, B.H., 2000. An experimental and computational study of multiphase flow behaviour in a circulating fluidized bed, *Int. Journal of Multiphase Flow*, 26, 387-419
14. Olsson, S.E., and Almstedt, A.E., 1995. Local instantaneous and time-averaged heat transfer in a pressurized fluidized bed with horizontal tubes: Influence of pressure, fluidization velocity and tube-bank geometry, *Chem. Engng. Sci* ., 50, 3231-3245
15. Patil, D.J., Smit. J., M. van Sint Annaland, and Kuipers, J.A.M., 2006. Wall-to-bed heat transfer in gas–solid bubbling fluidized beds, *AIChE J.*, 52, 58-74

16. Roffel, B., and Chin, P., 1987. Computer Control in the Process Industries, Chealsea, MI: Lewis Publishers

17. Seborg, D.E., Edgar, T.F., and Mellichamp, D.A., 2004. Process dynamics and control, John Wiley and Sons, Inc.

18. Schaeffer, D.G., 1987. Instability of evolution equations describing incompressible granular flow, *J. Differ. Eqs.*, 66, 19

19. Schmidt, A., and Renz, U., 1999. Eulerian computation of heat transfer in fluidized beds, *Chem. Engng. Sci.*, 54, 5515-5522

20. Schmidt, A., and Renz, U., 2005. Numerical prediction of heat transfer between a bubbling fluidized bed and an immersed tube bundle, *Heat and Mass Transfer,* 41, 257-270

21. Sinclair, J. L., and Jackson, R., 1989. Gas-particle flow in a vertical pipe with particle-particle interactions, *AIChE J.*, 35, 1473-1486

22. Srivastava, A., and Sundaresan, S., 2003. Analysis of a frictional-kinetic model for gas-particle flow, *Powder Technol.*, 129, 72-85

23. Wiman, J., Mahpour, B., and Almstedt, A.E., 1995. Erosion of horizontal tubes in a pressurised fluidized bed: influence of pressure, fluidization velocity and tube-bank geometry, *Chem. Engng. Sci.*, 50, 3345-3356

24. Wiman, J., and Almstest, A.E., 1997. Hydrodynamics, erosion and heat transfer in a pressurised fluidized bed: influence of pressure, fluidization velocity, particle size and tube bank geometry, *Chem. Engng. Sci.*, 52, 2677-2695

25. Xie, N., Battaglia, F., and Pannala, S., 2008a. Effect of using two- versus three-dimensional modelling of fluidized beds, Part 1 hydrodynamics, *Powder Technol.*, 182, 1-13

26. Xie, N., Battaglia, F., and Pannala, S., 2008b. Effect of using two- versus three-dimensional modelling of fluidized beds, Part 2 budget analysis, *Powder Technol.*, 182, 14-24

27. Yurong, H., Huilin, L., Qiaoqun, S., Lidan, Y., Yunhua, Z., Gidaspow, D., and Bouillard, J., 2004. Hydrodynamics of gas-solid flow around immersed tubes in bubbling fluidized beds, *Powder Technol.*, 145, 88-105

28. Yusuf, R., Melaaen, M. C., and Mathiesen, V., 2005. Convective heat and mass transfer modelling in gas-fluidized beds, *Chem. Engng. Technol.*, 28, 13-24

29. Yusuf, R., Halvorsen, B., and Melaaen, M.C., 2008. An experimental and computational study of wall to bed heat transfer in a bubbling fluidized bed, to be communicated to *Int. J. Multiphase Flow*

30. Zehner, P., and Schluender, E.U, 1970. Warmeleitfaehig eit von schuettungen bei maessignen temperaturen, *Chemie Ing. Techn.*, 42, 933-941